# Multiscale Model for Solid Oxide Fuel Cell with Electrode Containing Mixed Conducting Material

**Daifen Chen**
School of Energy and Power Engineering, Jiangsu University of Science and Technology, Zhenjiang 212003, China

Dept. of Chemical Engineering, Curtin University, WA 6845, Australia

**Hanzhi Wang and Shundong Zhang**
School of Energy and Power Engineering, Jiangsu University of Science and Technology, Zhenjiang 212003, China

**Moses O. Tade and Zongping Shao**
Dept. of Chemical Engineering, Curtin University, WA 6845, Australia

**Huili Chen**
Dept. of Chemical Engineering, Curtin University, WA 6845, Australia

Institute of Molecular Science, Shanxi University, Taiyuan 030006, China

*DOI 10.1002/aic.14881*
*Published online June 5, 2015 in Wiley Online Library (wileyonlinelibrary.com)*

*Solid oxide fuel cells (SOFCs) with electrodes that contain mixed conducting materials usually show very different relationships among microstructure parameters, effective electrode characteristics, and detailed working processes from conventional ones. A new multiscale model for SOFCs using mixed conducting materials, such as LSCF or BSCF, was developed. It consisted of a generalized percolation micromodel to obtain the electrode properties from microstructure parameters and a multiphysics single cell model to relate these properties to performance details. Various constraint relationships between the activation overpotential expressions and electric boundaries for SOFC models were collected by analyzing the local electrochemical equilibrium. Finally, taking a typical LSCF-SDC/SDC/Ni-SDC intermediate temperature SOFC as an example, the application of the multiscale model was illustrated. The accuracy of the models was verified by fitting 25 experimental I-V curves reported in literature with a few adjustable parameters; additionally, and several conclusions were drawn from the analysis of simulation results.* © 2015 American Institute of Chemical Engineers *AIChE J*, 61: 3786–3803, 2015

*Keywords: mixed ion-electron conductor, percolation theory, COMSOL multiphysics model, electrochemical reaction, electronic current leakage*

## Introduction

Solid oxide fuel cells (SOFC) have been recognized as a promising energy conservation technology in terms of cleanliness, efficiency, and capability to work with various types of fuels.[1–7] However, high operating temperature cause strict material compatibility constraints, cost limitation, and challenging operational complexity.[1] Thus, increasing attention has been devoted to the development of intermediate temperature (500–700°C) SOFC (IT-SOFC) components.[8–10] The key obstacles to the reduction of the SOFC operation temperature are the insufficient activity of conventional cathode materials for oxygen reduction reaction and the low ionic conductivity of the traditional electrolyte materials (YSZ) in this temperature regime. Thus, mixed ion/$e^-$ conducting (MIEC) electrode materials (e.g., LSCF, $CeO_2$, LSCM, SFMO, BSCF) and alternative electrolyte materials (i.e., SDC and GDC) have received great attention for their potential applications in IT-SOFC.[11] Shao et al.[3] proposed a mixed conducting $Ba_{0.5}Sr_{0.5}Co_{0.8}Fe_{0.2}O_{3-\delta}$ as a potential cathode material in IT-SOFC. In principle, the reaction sites in mixed conducting electrodes are very different from those in the conventional composite (or pure electronic) electrodes. Taking the cathode as an example, the potential electrochemically active sites (PEAS) extend from the percolated three phase boundary sites (TPBs) over the electrode/dense electrolyte interface for the pure LSM electrode, through the percolated volume TPBs (e.g., LSM-YSZ-pores) within the conventional LSM-YSZ

Additional Supporting Information may be found in the online version of this article.

Correspondence concerning this article should be addressed to Z. Shao at shaozp@njtech.edu.cn; zongping.shao@curtin.edu.au.

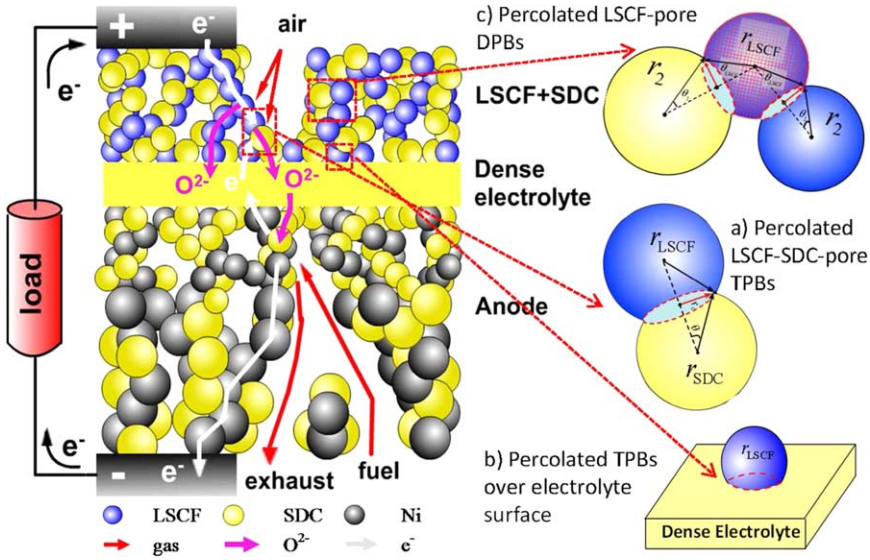


**Figure 1. Illustrations of the microstructure diagram and physical-chemical processes within a typical LSCF-SDC/SDC/Ni-SDC IT-SOFC.**

**Red dashes indicate three different PEAS on cathode side. [Color figure can be viewed in the online issue, which is available at wileyonlinelibrary.com.]**

electrode, to the percolated volume double phase boundary sites (DPBs) (e.g., LSCF-pore or BSCF-pore) within the mixed conducting electrode. Here, "percolated" is defined as exhibiting a continuous connection through the entire electrode structure; Recently, an *in situ* photoelectron spectroscopy method was proposed to investigate the electrochemically active region within the mixed conducting $CeO_{2-x}$ electrode.[12] The LSCF coated with SDC was proposed by Xia and coworkers[13] to investigate the surface exchange coefficient of LSCF/SDC interface using the electrical conductivity relaxation method. Wang et al.[14] compared the performances of various LSCF-based cathodes and found surprisingly, that the LSCF-SDC composite cathode exhibited a larger activation overpotential than did the single-phase LSCF cathode. More interestingly, the LSM-coated LSCF composite electrode was reported to exhibit a lower, instead of higher, activation overpotential compared with that of a pure LSCF cathode.[14] All of the experimental results mentioned above suggest that a complicated oxygen reaction mechanism is present in electrodes using mixed conducting materials.

As the art of the IT-SOFC electrode fabrication technologies become sophisticated, more functions are required from the electrode structure to achieve a high SOFC performance; there is an increasing need to understand the relationships among the microstructure parameters, effective electrode characteristics, and the detailed chemical and physicals processes in SOFCs.[15–19] However, to the best of our knowledge, only few works have focused on the numerical modeling studies relevant for these SOFCs. For example, an analytical model was developed by Leah et al. to study the electronic current leakage within a metal-supported SOFC using GDC as the dense electrolyte.[20] A 2-D isothermal mathematical model for a dense SDC electrolyte was then developed, and it was found that the rate of leakage current increases with the increasing operating voltage, temperature, and hydrogen concentration in the fuel stream.[21] Recently, an analytical model was developed by Shen et al. to describe the current leakage process within a bilayer electrolyte.[22] However, most of these early theoretical works have focused on the electric leakage phenomenon based on only part of the cell structure. Both the IT-SOFC electrode and electrolyte materials may have many different characteristics from those of their counterparts in conventional SOFCs, because of the use of mixed conducting materials and presence of electronic conducting capability for dense electrolyte materials (e.g., SDC and CGO). These may lead to very different relationships among the electrode microstructure parameters, effective electrode characteristics, and the detailed working processes. Taking the LSCF-SDC/SDC/NI-SDC IT-SOFC as an example, Figure 1 shows the conceptual illustration of the microstructure diagram and physical-chemical processes: (1) because the LSCF-conductor on cathode side shows mixed conducting properties, both LSCF- and SDC-conductors will contribute to the alternative $O^{2-}$ conducting paths; (2) the $e^-$ charge can be conducted from anode to the cathode side through the dense SDC electrolyte directly, which lead to a continuous electronic potential distribution throughout the whole cell structure; and (3) the PEASs are very different from those for the conventional electrode, such as the percolated volume LSCF-SDC-pore TPBs (Figure 1a), percolated TPBs over dense electrolyte surface (Figure 1b), and percolated volume LSCF-SDC DPBs (Figure 1c). Which and how much part of these PEASs can be real electrochemical active sites (EAS) are further determined by the balance among the local electrochemical activation polarization and the species, $e^-$ and ionic transporting resistances to achieve the minimal total potential loss. These further depend on the detailed electrode composition, microstructure parameters, and operating conditions. Therefore, although it is difficult to comprehensively consider these characteristics using the multiscale model, it is essential to understand the effects of IT-SOFC material compositions and microstructure parameters on the macroelectrode characteristic properties; and further on the detailed working processes.

In this article, the detail electrochemical reaction, electric leakage, and $e^-$, ion and gas transporting processes in the typical IT-SOFC are analyzed and illustrated schematically using

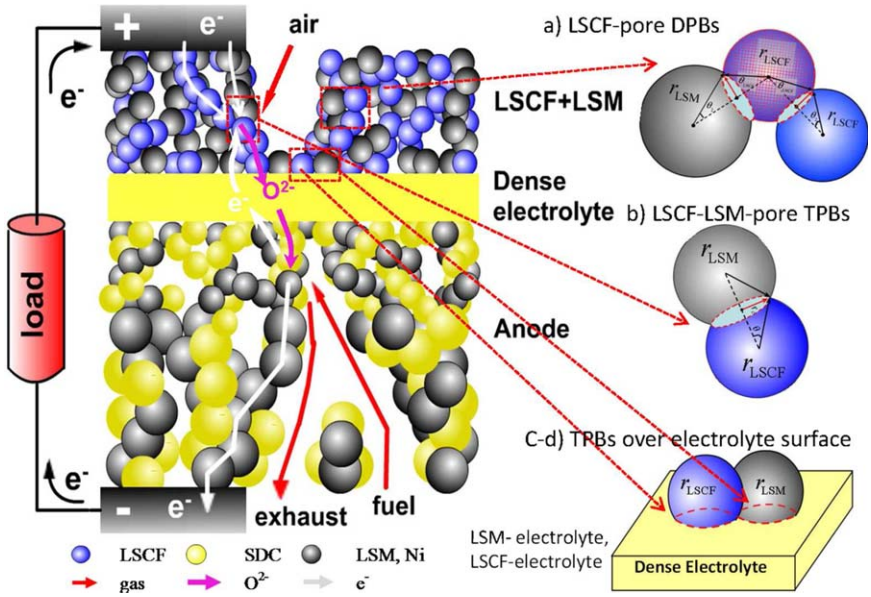


**Figure 2. Illustrations of the microstructure diagram and physical-chemical processes within a typical LSCF-LSM/SDC/Ni-SDC IT-SOFC.**

**Red dashes indicate four different PEAS on cathode side. [Color figure can be viewed in the online issue, which is available at wileyonlinelibrary.com.]**

an equivalent circuit approach to provide a way to easily understand the specific characteristics and complicated chemical and physical processes. As there is continuous electronic potential distribution throughout the entire cell structure, proper constraint relationships between the activation overpotential expressions and electric boundary settings are obtained by carefully analyzing the local electrochemical equilibrium process. It can be an important reference for the proper boundary settings in different SOFC models. Taking LSCF-SDC/SDC/Ni-SDC cells as an example, a multiscale predictive models that comprehensive considers these special characteristics for the typical mixed conducting SOFCs is developed. The generalized percolation micromodel is used to evaluate the characteristic properties of each SOFC component from the microstructure parameters. Based on these properties, the macroscale single cell model is developed to predict the working details within the cells. The effects of electronic current leakage on the open circuit voltage (OCV) and operating performance are studied as well. Finally, the accuracy of the developed multiscale models is verified by comparing the calculated results with the 25 experimental *I-V* curves obtained from literature. Such verified multiscale models are not limited to the LSCF-SDC/SDC/Ni-SDC, can greatly enhance our understanding of the IT-SOFC, and are essential for the further investigations of the effects of the electrode microstructures on the IT-SOFC performances, identification of guidelines for SOFC performance optimization.

## Theory and Numerical Model

Taking the typical LSCF-SDC/SDC/Ni-SDC IT-SOFC as an example, the development and application of the multiscale models for SOFCs using MIEC materials are illustrated. It is necessary to note that the applications of the developed multiscale models are not limited to the LSCF-SDC/SDC/Ni-SDC IT-SOFC, and they can also be applied to describe other SOFCs using different electrode compositions and mixed conducting materials.

As shown in Figure 1, a typical LSCF-LSM/SDC/Ni-SDC IT-SOFC consists of three layers: (a) a porous Ni-SDC composite anode layer with Ni- and SDC-particles; (b) a dense SDC electrolyte layer; and (c) a porous LSCF-SDC composite cathode layer with LSCF- and SDC-particles. Taking hydrogen as fuel and air as an oxidant as an example, the elementary electrochemical $e^-$-ion charge transfer reaction based on $O^{2-}$ can be described as

$$\text{Anodic reaction}: H_2(\text{pore}) + O^{2-}(\text{SDC}) \rightarrow H_2O(\text{pore}) + 2e^-(\text{Ni}) \quad (1)$$

$$\text{Cathodic reaction}: 0.5O_2(\text{pore}) + 2e^-(\text{LSCF}) \rightarrow O^{2-}(\text{SDC or LSCF}) \quad (2)$$

where the information in the parentheses indicate the located positions of the reactants.

### *The potential electrochemical active sites*

According to Eqs. 1 and 2, the elementary $e^-$-$O^{2-}$ charge transfer reaction simultaneously involves electrons, ions, and gases, and these reactants are located at different material phases. Thus, the coexisting sites of the percolated gas transporting, electronic conducting, and ionic conducting paths are essential for the electrochemically active reaction. As shown in Figures 1 and 2, different PEASs and activities are obtained based on different IT-SOFC electrode compositions,

1. for LSCF-SDC composite cathode in Figure 1, because both LSCF- and SDC-materials contribute to the $O^{2-}$ transport, there are three different types of PEASs, (a) the percolated LSCF-SDC-pore TPBs within the composite cathode shown in Figure 1a. Here, the TPBs means the coexist sites among three different material phases (i.e., pore, LSCF- and SDC-material phases); (b) the percolated LSCF-pore DPBs between the mixed conducting material (i.e., LSCF) and

pores within the composite cathode shown in Figures 1c; and (c) the percolated TPBs over the dense electrolyte surface shown in Figure 1b;

2. for the pure LSCF cathode layer, however, there are only two types of PEASs: (a) the percolated LSCF-pore DPBs; and (b) the percolated TPBs over the dense electrolyte surface;

3. for a typical Ni-SDC composite anode in Figure 1, the PEASs consist of (a) the percolated Ni-SDC-pore TPBs within the composite anode; and (b) the percolated TPBs over the dense electrolyte surface;

4. for LSCF-LSM composite cathode in Figure 2, as both LSCF- and LSM-material phases contribute to the electronic conducting path, there are four types of PEASs: (a) the percolated LSCF-pore DPBs within the cathode shown in Figure 2a; (b) the percolated LSCF-LSM-pore TPBs within the cathode shown in Figure 2b; and (c) and (d) the percolated TPBs over the dense electrolyte surface (i.e., both LSCF-electrolyte and LSM-electrolyte intersections), as shown in Figures 2c, d, respectively.

### *The equivalent circuit of electric processes within the IT-SOFC*

The physical and chemical processes within the typical LSCF-SDC/SDC/Ni-SDC IT-SOFC are simply shown in Figure 1. The white, purple, and red arrows indicate the relevant $e^-$, $O^{2-}$, and gas transport paths, respectively. On the anode side, fuel from the anode gas channel is transported through the porous anode structure to the percolated Ni-SDC-pore TPB sites. Around these sites, the fuel is oxidized by oxygen ions ($O^{2-}$), as specified in Eq. 1. The product $H_2O$ is transported back to the fuel channel through the porous anode structure. Most produced $e^-$ are conducted to the cathode side through the electronic conducting paths within the anode and the external circuit to provide useful electric power. A fraction of the produced $e^-$ will conduct to the cathode reaction sites directly through the dense electrolyte, because the electronic conductivity of the dense SDC electrolyte cannot be negligible.[23] Because these electrons do not flow through the external circuit, they are considered be consumed.

On the cathode side, air from the cathode channel is transported through the gas path to the cathode PEASs (i.e., the percolated volume LSCF-SDC-pore TPBs and LSCF-pore DPBs and the percolated TPBs over the dense electrolyte surface). At these sites, $O_2$ reacts with the $e^-$ from both the external circuit and the dense electrolyte. The product $O^{2-}$ are then conducted to the anode electrochemical reaction sites by the ion conducting SDC- (or LSCF-) paths within the cathode and dense electrolyte.

To further carefully understand the electronic and ionic conductions and the electrochemical reaction processes, the equivalent circuit corresponding to the LSCF-SDC/SDC/Ni-SDC is presented in Figure 3. Dark bricks indicate the electronic conduction path formed by LSCF- (or Ni-) particles. Light and blue colored bricks represent the ionic conduction paths constructed by the SDC- and LSCF-particles, respectively. The parallel circuits within the black, red, and blue dashed panes represent the local percolated LSCF-SDC-pore (or Ni-SDC-pore) TPBs within the composite electrode, the percolated TPBs over the dense electrolyte surface, and the percolated LSCF-pore DPBs within the composite cathode. These PEASs are the alternative $e^-$-$O^{2-}$ charge transfer reaction paths. Generally, it is reasonable to represent these reaction paths by the parallel circuits that consist of electromotive

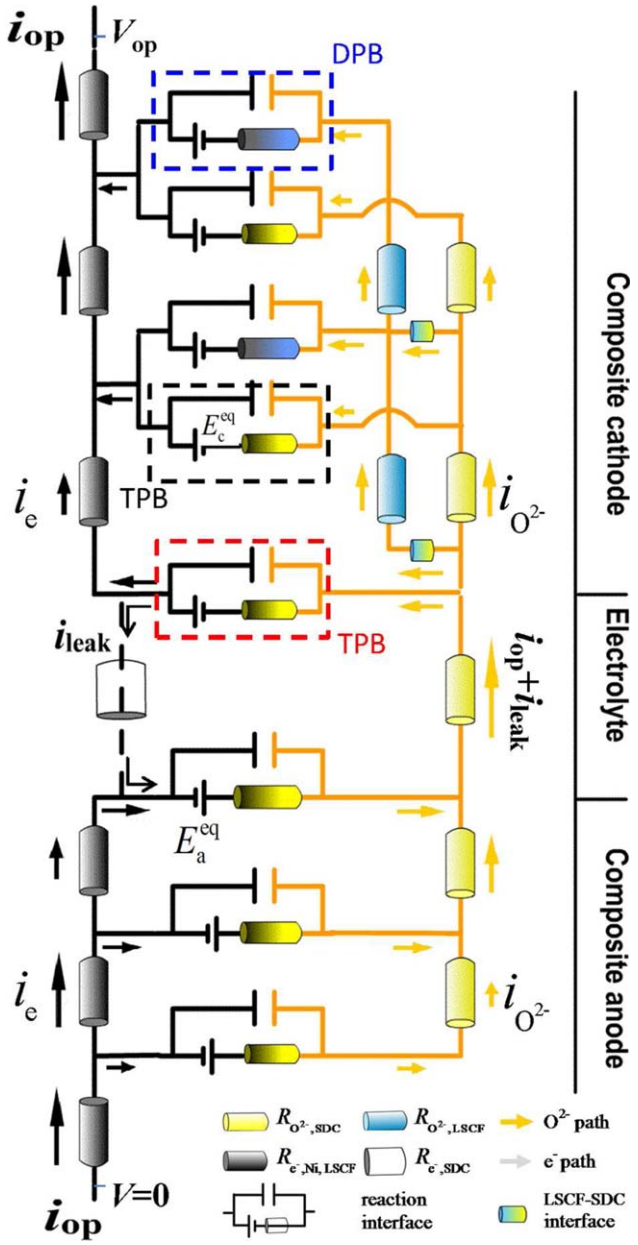


**Figure 3. The equivalent circuit of the electric process within LSCF-SDC/SDC/Ni-SDC SOFC.**

**Parallel circuits within the black, red, and blue dashed panes represent the local percolated volume LSCF-SDC-pore TPBs, percolated TPBs over dense electrolyte surface, and percolated LSCF-pore DPBs. $E_a^{eq}$ and $E_c^{eq}$ are the local equilibrium electric potential differences. [Color figure can be viewed in the online issue, which is available at wileyonlinelibrary.com.]**

forces, capacitors, and resistors.[24,25] Electromotive forces $E_a^{eq}$ and $E_c^{eq}$ are the local equilibrium electric potentials difference between the electronic and ionic conducting phases. $i_{op}$, $i_{leak}$, $i_e$, and $i_{O^{2-}}$ are the output current density, electronic current due to internal leakage, local electronic, and ionic current densities, respectively. It is necessary to note that due to the negative charge of $e^-$ and $O^{2-}$, the electronic (or ionic) current flows in the opposite directions of $e^-$ (or $O^{2-}$) charge flows.

$i_{op}$ flows from the anode interconnect to the composite anode and is converted into the ionic electric current $i_{O^{2-}}$ by the elementary $e^-$-$O^{2-}$ charge transfer reaction around the

percolated Ni-SDC-pore TPBs. There are parallel paths for the electronic and ionic current conductions within the composite anode to convert $i_e$ into $i_{O^{2-}}$ gradually. Both the anode electronic current and the leaked electronic current from dense SDC electrolyte are converted into $i_{O^{2-}}$ before entering the dense electrolyte. In other words, all of the produced $O^{2-}$ should flow through the dense electrolyte. The total flow is given by the sum of $i_{op}$ and $i_{leak}$, which should be used to calculate the total fuel and oxygen consumptions.

The $i_{O^{2-}}$ is transported through the dense electrolyte to the LSCF-SDC composite cathode, where the $O^{2-}$ will be converted back into the $i_e$ through the $e^-$-$O^{2-}$ charge transfer paths. It should be noted that there are, (1) two parallel ionic conduction paths formed by both the LSCF- and SDC-particles, (2) one electronic conduction path formed by the LSCF-particles, and (3) three different alternative $e^-$-$O^{2-}$ charge transfer reaction paths (i.e., percolated volume LSCF-SDC-pore TPBs, percolated TPBs over the dense electrolyte surface, and percolated LSCF-pore DPBs). Generally, the paths with minimal overall potential losses would be chosen for the interconversion of the $O^{2-}$ and $e^-$ charges and their transport through the entire cathode structure. Most of the produced $i_e$ is transported back to the anode reaction sites through the electronic conduction paths within the cathode, the cathode interconnect, and the external load. Because of the nonzero electronic conductivity of the dense SDC electrolyte, a fraction of the produced $e^-$ current leaks through the dense electrolyte to the anode TPB sites. As $i_{leak}$ does not flow through the external load, it is considered to be consumed. In conclusion, the equivalent circuit model can be used to accurately depict the detailed electrical processes within the typical LSCF-SDC/SDC/Ni-SDC IT-SOFC.

### *The real EAS*

The analysis in Figure 3 shows that the paths with minimal overall potential losses would be chosen for the interconversion of the $O^{2-}$ and $e^-$ charges and their transport throughout the entire cathode structure. The overall potential losses consist of the local anode/cathode electrochemical activation polarizations and the transporting resistances of species, $e^-$, and ions. Thus, the sites common to the percolated $e^-$, ionic, and gas transporting paths shown in Figure 1 are only the PEASs. Which and how much part of these PEASs can be the EAS depends on the following factors:

1. the $e^-$ conductivity capability from the interconnect into the electrode structure (shown as white path in Figure 1), This can be described by the effective electronic conductivity based on the component geometry $\sigma_e^{eff}$ and is determined by the electrode composition, microstructure parameters, intrinsic properties of each material and operating conditions;

2. the ion propagating capability from the dense electrolyte surface into the composite electrode (shown as the purple paths in Figure 1). This is described by the effective ionic conductivity $\sigma_{O^{2-}}^{eff}$ based on the component geometry. For LSCF-SDC cathode in Figure 1, both LSCF- and SDC-conductors contribute to the high effective $O^{2-}$ conductivity;

3. the capability for species transport from the cell channels into the porous electrode structure (shown as the red path within Figure 1). This is described by the effective diffusivities of each species within the porous electrode structure $D_\alpha^{eff}$ and is controlled by the gas mixture composition, intrinsic properties of each gas, porosity, hydraulic pore radius, and tortuosity of the gas flow path;

4. the electrochemical activities around various PEASs. These are described by the local exchange transfer current rates, activation energies, and forward/reverse reaction symmetric factors around each type PEAS. For LSCF-SDC composite cathode in Figure 1, three types of PEASs are present and possess very different capabilities for electrochemical activity;

5. the thickness of the specific composite electrode and the operating conditions are also important factors that affect the EAS distribution within these SOFCs.

Generally, most of the effective characteristics described above are affected by the details of electrode composition, microstructure parameters, and operating conditions. Taking the LSCF-SDC composite cathode as an example, the relevant PEAS and EAS distributions for three different representative LSCF-loading scenarios are illustrated in Supporting Information.

### *Mathematical description for the local electrochemical equilibrium process*

According to the anodic $e^-$-$O^{2-}$ charge transfer reaction in Eq. 1, the reactant electrochemical potentials should be balanced at the equilibrium state (no net reaction case) to obtain[26]

$$\mu_{H_2}+\mu_{O^{2-}}-2F\Phi_{O^{2-}}^{eq}=\mu_{H_2O}-2F\Phi_e^{eq}\ (\mathrm{J}) \tag{3}$$

$$E_a^{eq}=\Phi_{O^{2-}}^{eq}-\Phi_e^{eq}=\frac{1}{2F}\left(\mu_{H_2}+\mu_{O^{2-}}-\mu_{H_2O}\right)(\mathrm{V}) \tag{4}$$

where $\mu_\alpha$ is the chemical potential of reactant $\alpha$. It can be evaluated as $\mu_\alpha=\mu_\alpha^{st}+RT\ln p_\alpha$, where $\mu_\alpha^{st}$ is the chemical potential at standard condition ($p^{st}=1$ atm). $T$ is the local temperature, and $p_\alpha$ is the partial pressure of species $\alpha$ at the local sites. $F$ is the Faraday constant defined as the electric charge carried by one mole of electrons. $\Phi_{O^{2-}}^{eq}$ and $\Phi_e^{eq}$ are the local equilibrium electrical potentials at the ionic and electronic conducting phases, respectively. The local anode equilibrium electric potential difference $E_a^{eq}$ between two conducting phases then achieved by Eq. 4. We note that $E_a^{eq}$ is evaluated based on the operating conditions instead of the open circuit conditions and is considered the local electromotive force in Figure 3.

However, for the actual operating process that produces nonzero electric current, the electrochemical potential at the left side of Eq. 1 should larger than that at the right side

$$\mu_{H_2}+\mu_{O^{2-}}-2F\Phi_{O^{2-}}>\mu_{H_2O}-2F\Phi_e\ (\mathrm{J}) \tag{5}$$

$$\begin{aligned}\eta_{act}^a&=E_a^{eq}-\left(\Phi_{O^{2-}}-\Phi_e\right)\\&=\frac{1}{2F}\left(\mu_{H_2}+\mu_{O^{2-}}-\mu_{H_2O}\right)-\left(\Phi_{O^{2-}}-\Phi_e\right)(\mathrm{V})\end{aligned} \tag{6}$$

In this case, the actual local ionic and electronic electric potentials, $\Phi_{O^{2-}}$ and $\Phi_e$, should shift from their respective equilibrium values at the equilibrium state, $\Phi_{O^{2-}}^{eq}$ and $\Phi_e^{eq}$. Such shift is defined as the local anode activation overpotential as Eq. 6.

Generally, for the PEAS located around the percolated Ni-SDC-pore TPBs, the $e^-$-$O^{2-}$ charge transfer rate per unit TPB length $j_{TPB}$ (A m$^{-1}$) can be evaluated as a function of $\eta_{act}$ using the empirical Butler–Volmer equation as[24]

$$j_{TPB}=j_{TPB,0}\left[\exp\left(\frac{2\alpha_f F}{RT}\eta_{act}\right)-\exp\left(-\frac{2\beta_r F}{RT}\eta_{act}\right)\right](\mathrm{A\,m^{-1}}) \tag{7}$$

where $R$ is the universal gas constant. $\alpha_f$ and $\beta_r$ are the forward and reverse reaction symmetric factors, respectively. The local

**Table 1. Collection of Different Electric Potential Shift Assumptions and the Relevant Constraint Relationships Between Activation Overpotential Expressions and Electric Boundary Settings**

| | $\hat{\Phi}_e^a$, $\hat{\Phi}_e^c$, $\hat{\Phi}_{O^{2-}}$ | $\eta_{act}^a$, $\eta_{act}^c$ | $\Phi_e^c\|_{B6}$, $\Phi_e^a\|_{B1}$ |
|---|---|---|---|
| Origin | $\Phi_e$<br>$\Phi_{O^{2-}}$ | $\eta_{act}^a = E_a^{eq} - (\Phi_{O^{2-}} - \Phi_e)$<br>$\eta_{act}^c = E_c^{eq} - (\Phi_e - \Phi_{O^{2-}})$ | $\Phi_e^c\|_{B6} - \Phi_e^a\|_{B1} = V_{op}$<br>$\Phi_e^c\|_{B6} = V_{op}$<br>$\Phi_e^a\|_{B1} = 0$ |
| Assumption 1[25,29] | $\hat{\Phi}_e^a = \Phi_e + \frac{1}{2F}(\mu_{H_2}^0 - \mu_{H_2O}^0)$<br>$\hat{\Phi}_e^c = \Phi_e - \frac{1}{4F}\mu_{O_2}^0$<br>$\hat{\Phi}_{O^{2-}} = \Phi_{O^{2-}} - \frac{1}{2F}\mu_{O^{2-}}$ | $\eta_{act}^a = \hat{\Phi}_e^a - \hat{\Phi}_{O^{2-}} - \frac{RT}{2F}\ln\frac{p_{H_2}^0 p_{H_2O}}{p_{H_2} p_{H_2O}^0}$<br>$\eta_{act}^c = \hat{\Phi}_{O^{2-}} - \hat{\Phi}_e^c - \frac{RT}{4F}\ln\frac{p_{O_2}^0}{p_{O_2}}$ | $\hat{\Phi}_e^c\|_{B6} - \hat{\Phi}_e^a\|_{B1} = V_{op} - E_0$<br>$\hat{\Phi}_e^c\|_{B6} = V_{op}$<br>$\hat{\Phi}_e^a\|_{B1} = E_0$ |
| Assumption 2[18,30] | $\hat{\Phi}_e^a = \Phi_e + \frac{1}{2F}(\mu_{H_2}^{st} - \mu_{H_2O}^{st})$<br>$\hat{\Phi}_e^c = \Phi_e - \frac{1}{4F}\mu_{O_2}^{st}$<br>$\hat{\Phi}_{O^{2-}} = \Phi_{O^{2-}} - \frac{1}{2F}\mu_{O^{2-}}$ | $\eta_{act}^a = \hat{\Phi}_e^a - \hat{\Phi}_{O^{2-}} - \frac{RT}{2F}\ln\frac{p_{H_2O}}{p_{H_2}}$<br>$\eta_{act}^c = \hat{\Phi}_{O^{2-}} - \hat{\Phi}_e^c - \frac{RT}{4F}\ln\frac{1\text{ atm}}{p_{O_2}}$ | $\hat{\Phi}_e^c\|_{B6} - \hat{\Phi}_e^a\|_{B1} = V_{op} - E^{st}$<br>$\hat{\Phi}_e^c\|_{B6} = V_{op}$<br>$\hat{\Phi}_e^a\|_{B1} = E^{st}$ |
| Assumption 3[28] | $\Phi_e$<br>$\hat{\Phi}_{O^{2-}} = \Phi_{O^{2-}} - \frac{1}{2F}\mu_{O^{2-}}$ | $\eta_{act}^a = \Phi_e - \hat{\Phi}_{O^{2-}} + \frac{\mu_{H_2}^{st} - \mu_{H_2O}^{st}}{2F} - \frac{RT}{2F}\ln\frac{p_{H_2O}}{p_{H_2}}$<br>$\eta_{act}^c = \hat{\Phi}_{O^{2-}} - \Phi_e + \frac{\mu_{O_2}^{st}}{4F} - \frac{RT}{4F}\ln\frac{1\text{ atm}}{p_{O_2}}$ | $\Phi_e^c\|_{B6} - \Phi_e^a\|_{B1} = V_{op}$<br>$\Phi_e^c\|_{B6} = V_{op}$<br>$\Phi_e^a\|_{B1} = 0$ |
| Assumption 4 | $\Phi_e$<br>$\hat{\Phi}_{O^{2-}} = \Phi_{O^{2-}} + \frac{1}{4F}(\mu_{O_2}^{st} - 2\mu_{O^{2-}})$ | $\eta_{act}^a = \Phi_e - \hat{\Phi}_{O^{2-}} + E^{st} - \frac{RT}{2F}\ln\frac{p_{H_2O}}{p_{H_2}}$<br>$\eta_{act}^c = \hat{\Phi}_{O^{2-}} - \Phi_e - \frac{RT}{4F}\ln\frac{1\text{ atm}}{p_{O_2}}$ | $\Phi_e^c\|_{B6} - \Phi_e^a\|_{B1} = V_{op}$<br>$\Phi_e^c\|_{B6} = V_{op}$<br>$\Phi_e^a\|_{B1} = 0$ |

Note: $E_0 = \frac{1}{2F}\left(\mu_{H_2}^0 + 0.5\mu_{O_2}^0 - \mu_{H_2O}^0\right) = \frac{\Delta\mu^{st}}{2F} + \frac{RT}{2F}\ln\frac{p_{H_2}^0 (p_{O_2}^0)^{0.5}}{p_{H_2O}^0}$ is the Nernst potential based on species concentrations on the channel inlets.
$E_0^{st} = \frac{1}{2F}\left(\mu_{H_2}^{st} + \frac{1}{2}\mu_{O_2}^{st} - \mu_{H_2O}^{st}\right) = \frac{\Delta\mu^{st}}{2F}$ is the Nernst potential at standard state (1 atm).

exchange transfer current per unit TPB length at the anode side can be expressed as[27,28]

$$j_{TPB,0}^a = j_{TPB,0,ref}^a \exp\left(-\frac{E_{H_2}}{R}\left(\frac{1}{T} - \frac{1}{T_{ref}}\right)\right)\left(\frac{p_{H_2} p_{H_2O}}{p_{H_2}^0 p_{H_2O}^0}\right)\ (\text{A m}^{-1}) \tag{8}$$

where $E_{H_2}$ is the activation energy for $H_2$ oxidation reaction. $j_{TPB,0,ref}^a$ is often assigned empirically at a reference temperature $T_{ref}$. $p_\alpha$ and $p_\alpha^0$ are the partial pressure of species $\alpha$ at the local site and channel inlet, respectively.

Similarly, the equilibrium electrochemical potentials for the oxygen reduction reaction in Eq. 2 can be written as Eq. 9. The equilibrium electric potential difference at the cathode between the electronic and ionic conducting phases can then be estimated by Eq. 10

$$0.5\mu_{O_2} - 2F\Phi_e^{eq} = \mu_{O^{2-}} - 2F\Phi_{O^{2-}}^{eq} \tag{9}$$

$$E_c^{eq} = \Phi_e^{eq} - \Phi_{O^{2-}}^{eq} = \frac{1}{4F}\left(\mu_{O_2} - 2\mu_{O^{2-}}\right)\ (\text{V}) \tag{10}$$

Due to the presence of the output electric current through the cell at operating conditions, the real local electric potentials, $\Phi_e$ and $\Phi_{O^{2-}}$, shift from their equilibrium values, $\Phi_e^{eq}$ and $\Phi_{O^{2-}}^{eq}$. The shift of the local potential difference is defined as the local cathode activation overpotential

$$\begin{aligned}\eta_{act}^c &= E_c^{eq} - (\Phi_e - \Phi_{O^{2-}}) \\ &= \frac{1}{4F}\left(\mu_{O_2} - 2\mu_{O^{2-}}\right) - (\Phi_e - \Phi_{O^{2-}})(\text{V})\end{aligned} \tag{11}$$

For the PEAS located around the percolated LSCF-SDC-pore TPBs, the $e^-$-$O^{2-}$ charge transfer rate per unit TPB length $j_{TPB}$ (A $m^{-1}$) can be similarly evaluated using Eq. 7. The relevant local exchange transfer current per unit TPB length on the cathode side can be estimated as[27,28]

$$j_{TPB,0}^c = j_{TPB,0,ref}^c \exp\left(-\frac{E_{O_2}}{R}\left(\frac{1}{T} - \frac{1}{T_{ref}}\right)\right)\left(\frac{p_{O_2}}{p_{O_2}^0}\right)^{0.25}\ (\text{A m}^{-1}) \tag{12}$$

where $E_{O_2}$ is the activation energy for the $O_2$ reduction reaction. $j_{TPB,0,ref}^c$ is assigned empirically at reference temperature $T_{ref}$.

For the PEAS located around the percolated LSCF-pore DPBs, the $e^-$-$O^{2-}$ charge transfer rate per LSCF-particle area can be analogously evaluated as

$$i_{LSCF} = i_{LSCF,0}\left[\exp\left(\frac{2\alpha_{LSCF}F}{RT}\eta_{act}^c\right) - \exp\left(-\frac{2\beta_{LSCF}F}{RT}\eta_{act}^c\right)\right]\ (\text{A m}^{-2}) \tag{13}$$

where $\alpha_{LSCF}$ and $\beta_{LSCF}$ are the forward and reverse reaction symmetric factors, respectively. The local exchange transfer

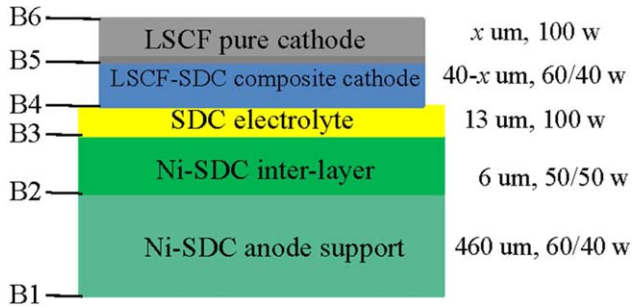


**Figure 4. The sketch figure of the typical IT-SOFCs with pure LSCF layer and LSCF-SDC composite cathode layer thicknesses as $x$ and $40-x$ μm to distinct five different cells in Table 2.**

**[Color figure can be viewed in the online issue, which is available at wileyonlinelibrary.com.]**

current based on per unit LSCF-particle surface area can be estimated as

$$i_{\mathrm{LSCF},0}=i_{\mathrm{LSCF},0,\mathrm{ref}}\exp\left(-\frac{E_{\mathrm{O_2}}}{R}\left(\frac{1}{T}-\frac{1}{T_{\mathrm{ref}}}\right)\right)\left(\frac{p_{\mathrm{O_2}}}{p^0_{\mathrm{O_2}}}\right)^{0.25}\ (\mathrm{A\,m^{-2}}) \tag{14}$$

where $i_{\mathrm{LSCF},0,\mathrm{ref}}$ is assigned empirically at the reference temperature $T_{\mathrm{ref}}$.

Thus, three different current sources/leakages can be obtained for the $e^-$ and $O^{2-}$ electric current conservation equations at the cathode side.

### *Proper constraint relationships between activation overpotentials and electric boundary settings*

Once the properties of each IT-SOFC component layer are assigned, all of the above equations, except $\mu_{O^{2-}}$ in Eqs. 6 and 11, can be solved using the local independent variables (e.g., $T$, $p_\alpha$, $\Phi_e$, and $\Phi_{O^{2-}}$). To conveniently solving the Butler–Volmer and overpotential expressions described above, the local electric potentials, $\Phi_e$ and $\Phi_{O^{2-}}$, should be shifted by a reference amount to overcome the effects of $\mu_{O^{2-}}$. Generally, the constant potential shift does not alter the electronic (or ionic) electric potential profiles within the electronic (or ionic) conducting phase. However, it is very important to note that the relevant overpotential expressions and electric boundary settings should be changed consistently to ensure the accuracy of the mathematical model. To the best of our knowledge, over the past decades, three shift assumptions for $\Phi_e$ and $\Phi_{O^{2-}}$ had been proposed and widely used in previous work by us and others.[25,28–30] These shift assumptions and the relevant constraint relationships are collected in Table 1. Here, $\hat{\Phi}^{a}_{e}|_{B1}$ and $\hat{\Phi}^{c}_{e}|_{B6}$ indicate the relevant boundary condition constraint of the electronic potentials at the anode/interconnect and cathode/interconnect interfaces, respectively.

It is necessary to note that for most of the convenient SOFC models that assumes that the dense electrolyte is an ideal electronic insulator, the $\Phi_e$ value at the anode and cathode sides were usually shifted by two different constant potentials as $\hat{\Phi}^{a}_{e}$ and $\hat{\Phi}^{c}_{e}$, respectively. However, because the electronic current leakage phenomenon at the dense SDC electrolyte is not ignored in the LSCF-SDC/SDC/Ni-SDC SOFC model in this article, there is a continuous $\Phi_e$ distribution throughout the whole cell structure. Therefore, the $\Phi_e$ value at both the anode and cathode sides should be either shifted by the same constant potential or left unchanged to preserve the electronic electric potential profiles within the cell. It is essential to develop an accurate IT-SOFC mathematical model. Assumption 4 in Table 1 is proposed and used, in which $\Phi_e$ is left unchanged and the local $\Phi_{O^{2-}}$ is shifted by a reference amount

$$\hat{\Phi}_{O^{2-}}=\frac{1}{4F}\left(\mu^{\mathrm{st}}_{\mathrm{O_2}}-2\mu_{O^{2-}}\right)+\Phi_{O^{2-}}\ (\mathrm{V}) \tag{15}$$

The expressions for the overpotential in Eqs. 6 and 11 should then be rewritten as

$$\begin{aligned}\eta^{a}_{\mathrm{act}}&=\frac{1}{2F}\left(\mu_{\mathrm{H_2}}+\mu_{O^{2-}}-\mu_{\mathrm{H_2O}}\right)\\&-\left[\hat{\Phi}_{O^{2-}}-\frac{1}{4F}\left(\mu^{\mathrm{st}}_{\mathrm{O_2}}-2\mu_{O^{2-}}\right)-\Phi_e\right]\\&=E^{\mathrm{st}}+(\Phi_e-\hat{\Phi}_{O^{2-}})-\frac{RT}{2F}\ln\frac{p_{\mathrm{H_2O}}}{p_{\mathrm{H_2}}}\ (\mathrm{V})\end{aligned} \tag{16}$$

$$\eta^{c}_{\mathrm{act}}=\hat{\Phi}_{O^{2-}}-\Phi_e-\frac{RT}{4F}\ln\frac{1\ \mathrm{atm}}{p_{\mathrm{O_2}}}\ (\mathrm{V}) \tag{17}$$

where $E^{\mathrm{st}}$ is the Nernst potential at standard state (1 atm). This can be easily calculated as a function of the operating temperature $T$.

As $\Phi_e$ in both the anode and cathode sides is not shifted, the electronic potential difference between the cathode/interconnect and anode/interconnect interfaces (B6 and B1) is equal to the output voltage $V_{\mathrm{op}}$ as

$$V_{\mathrm{op}}=\Phi_e|_{B6}-\Phi_e|_{B1}\ (\mathrm{V}) \tag{18}$$

Generally, these assumptions and their relevant constraints in Table 1 can be used as an important reference to check the setting accuracy of the SOFC mathematical models.

### *Multiphysics model for typical SOFC using mixed conducting materials*

To illustrate the application of the typical SOFC multiscale models, five different IT-SOFCs with LSCF-SDC composite (or pure LSCF) cathodes, as reported by Wang et al.,[14] are chosen to develop and validate the numerical models. Figure 4 shows schematic of these IT-SOFCs, where the thicknesses of the pure LSCF and LSCF-SDC composite cathode layers are $x$ μm and $40-x$ μm for the distinct five different cells in Table 2. The detail thicknesses, composition, and microstructure parameters of each component layers in different cells are presented in Table 3.

The electrochemical reactions are processed to produce the volumetric $e^-$-$O^{2-}$ charge transfer rates and the surface $e^-$-$O^{2-}$ charge transfer rates over the electrode/dense

**Table 2. Five IT-SOFCs with Different Pure LSCF and LSCF-SDC Composite Cathode Layer Thicknesses**

| Structure | Cell A | Cell B | Cell C | Cell D | Cell E |
|---|---|---|---|---|---|
| Pure LSCF layer $x$ μm | 40 μm | 30 μm | 20 μm | 10 μm | 0 μm |
| LSCF-SDC composite cathode layer | 0 μm | 10 μm | 20 μm | 30 μm | 40 μm |

**Table 3. Electrode Composition, Microstructure Parameters, and the Calculated Effective Characteristic Properties of Each IT-SOFC Component Layer**

| | Cathode Collector | Cathode Interlayer | Electrolyte | Anode Interlayer | Anode Supporter |
|---|---|---|---|---|---|
| Composition | LSCF | LSCF-SDC | SDC | Ni-SDC | Ni-SDC |
| Thickness ($\mu$m) | $x = 40,30, 20, 10, 0$[14] | $y = 1 - x$[14] | 13[14] | 6[14] | 460[14] |
| Mass ratio | | 60/40[14] | | 50/50[14] | 60/40[14] |
| Volume ratio | 1 | 61 | 1 | 0.45 | 0.55 |
| Specific area ($m^2\ g^{-1}$) | 5.4[14] | 5.4/6.2[14] | 6.2[14] | 3.4/6.2[14] | 3.4/6.2[14] |
| Particle diameter ($\mu$m) | 0.99[14] | 0.99/0.53[14] | 0.53[14] | 0.8/0.53[14] | 0.8/0.53[14] |
| $\phi_g$ | 45.5%[14] | 40.4%[14] | | 30% | 40% |
| $\sigma_e^{eff}$ ($S\ m^{-1}$) | $3.33 \times 10^4$, 700°C | $1.05 \times 10^4$, 700°C | 0.6212, 700°C | $4.03 \times 10^4$, 700°C | $1.64 \times 10^5$, 700°C |
| | $3.47 \times 10^4$, 650°C | $1.09 \times 10^4$, 650°C | 0.4102, 650°C | $4.13 \times 10^4$, 650°C | $1.68 \times 10^5$, 650°C |
| | $3.57 \times 10^4$, 600°C | $1.12 \times 10^4$, 600°C | 0.2575, 600°C | $4.23 \times 10^4$, 600°C | $1.72 \times 10^5$, 600°C |
| | $3.62 \times 10^4$, 550°C | $1.14 \times 10^4$, 550°C | 0.1523, 550°C | $4.32 \times 10^4$, 550°C | $1.76 \times 10^5$, 550°C |
| | $3.62 \times 10^4$, 500°C | $1.14 \times 10^4$, 500°C | 0.0838, 500°C | $4.42 \times 10^4$, 500°C | $1.80 \times 10^5$, 500°C |
| $\sigma_{O^{2-}}^{eff}$ ($S\ m^{-1}$) | 0.2842, 700°C | 0.3008, 700°C | 3.7047, 700°C | 0.3887, 700°C | 0.1928, 700°C |
| | 0.1458, 650°C | 0.1823, 650°C | 2.3534, 650°C | 0.2763, 650°C | 0.1346, 650°C |
| | 0.0681, 600°C | 0.1035, 600°C | 1.4149, 600°C | 0.1811, 600°C | 0.0869, 600°C |
| | 0.0286, 550°C | 0.0549, 550°C | 0.7969, 550°C | 0.1084, 550°C | 0.0515, 550°C |
| | 0.0107, 500°C | 0.0269, 500°C | 0.4151, 500°C | 0.0587, 500°C | 0.0277, 500°C |
| $r_g$ ($\mu$m) | 0.606 | 0.414 | | 0.298 | 0.362 |
| $\lambda_{TPB,eff}^{V}$ ($m^{-2}$) | | $3.62 \times 10^{12}$ | | $2.62 \times 10^{12}$ | $4.39 \times 10^{12}$ |
| $S_{es,LSCF}$ ($m^{-1}$) | $2.02 \times 10^6$ | $1.29 \times 10^6$ | | | |
| $\lambda_{TPB,eff}^{S}$ ($m^{-1}$) | $1.63 \times 10^6$ | $9.13 \times 10^5$ | | $4.96 \times 10^5$ | $1 \times 10^6$ |
| $\tau$ | 14 | 16 | | 14 | 14 |

electrolyte interface. These are viewed as the electric current sources/leaks to the electronic (or ionic) electric current conservation processes. The electronic and ionic electric potentials, $\Phi_e$ and $\hat{\Phi}_{O^{2-}}$, should obey the following charge conservation equations

$$\nabla \cdot i_e = \nabla \cdot \left(-\sigma_e^{eff} \nabla \Phi_e\right) = \begin{cases} i_{e\text{-}O^{2-},LSCF}^{V,c} & \text{in cathode current collector} \\ i_{e\text{-}O^{2-},TPB}^{V,c} + i_{e\text{-}O^{2-},LSCF}^{V,c} & \text{in cathode interlayer} \\ 0 & \text{in Electrolyte} \\ -i_{e\text{-}O^{2-},TPB}^{V,a} & \text{in anode} \end{cases} \tag{19}$$

$$\nabla \cdot i_{O^{2-}} = \nabla \cdot \left(-\sigma_{O^{2-}}^{eff} \nabla \hat{\Phi}_{O^{2-}}\right) = \begin{cases} -i_{e\text{-}O^{2-},LSCF}^{V,c} & \text{in cathode current collector} \\ -\left(i_{e\text{-}O^{2-},TPB}^{V,c} + i_{e\text{-}O^{2-},LSCF}^{V,c}\right) & \text{in cathode interlayer} \\ 0 & \text{in Electrolyte} \\ i_{e\text{-}O^{2-},TPB}^{V,a} & \text{in anode} \end{cases} \tag{20}$$

where $\sigma_e^{eff}$ and $\sigma_{O^{2-}}^{eff}$ are the effective electronic and ionic conductivities, respectively. $i_e$ and $i_{O^{2-}}$ are the local electronic and $O^{2-}$ electric current densities, respectively. As $\sigma_e^{eff}$ of the dense SDC electrolyte cannot be neglected,[31,32] in Eq. 19, the equation describing $i_e$ conservation in the dense electrolyte layer should also be solved to describe the electronic current leakage phenomenon.

For the LSCF-SDC composite cathode with a mixed conducting LSCF-conductor, $i_{e\text{-}O^{2-},TPB}^{V,c}$ ($A\ m^{-3}$) is the $e^-$-$O^{2-}$ charge transfer rate per unit volume based on percolated LSCF-SDC-pore TPBs

$$i_{e\text{-}O^{2-},TPB}^{V} = j_{TPB} \lambda_{TPB.eff}^{V}\ (A\,m^{-3}) \tag{21}$$

where $\lambda_{TPB.eff}^{V}$ is the percolated TPB lengths per unit volume ($m^{-2}$), as determined by the electrode composition and microstructure parameters. $j_{TPB}$ ($A\ m^{-1}$) is the $e^-$-$O^{2-}$ charge transfer rate per unit TPB length, as specified in Eq. 7.

$i_{e\text{-}O^{2-},LSCF}^{V,c}$ is the $e^-$-$O^{2-}$ charge transfer rate per unit volume based on the percolated LSCF-pore DPBs

$$i_{e\text{-}O^{2-},LSCF}^{V,c} = i_{LSCF} S_{es,LSCF}\ (A\,m^{-3}) \tag{22}$$

where $S_{es,LSCF}$ is the percolated LSCF-pore DPB areas per unit volume ($m^{-1}$) and is a function of the electrode microstructure parameters. $i_{LSCF}$ ($A\ m^{-2}$) is the $e^-$-$O^{2-}$ charge transfer rate per unit LSCF-particle surface area, as specified in Eq. 13.

In addition, the $e^-/O^{2-}$ electric sources/leaks at the cathode/electrolyte interface should also be considered at the relevant boundary conditions. The $e^-$-$O^{2-}$ charge transfer rate per

**Table 4. Boundary Condition Settings for Solving the Charge and Gas Transporting Processes**

| | B1 | B2 | B3 | B4 | B5 | B6 |
|---|---|---|---|---|---|---|
| Ionic charge balance | Insulation | Continuity | $-n\cdot i_{O^{2-}}=i^{S,a}_{e\text{-}O^{2-},TPB}$ | $-n\cdot i_{O^{2-}}=-i^{S,c}_{e\text{-}O^{2-},TPB}$ | Continuity | Insulation |
| Electronic charge balance | 0 | Continuity | $-n\cdot i_e=-i^{S,a}_{e\text{-}O^{2-},TPB}$ | $-n\cdot i_e=i^{S,c}_{e\text{-}O^{2-},TPB}$ | Continuity | $V_{op}$ |
| Mass balance | $c^0_{H_2}$ $c^0_{H_2O}$ | Continuity | $-n\cdot N_{H_2}=\frac{-i^{S,a}_{e\text{-}O^{2-},TPB}}{2F}$<br>$-n\cdot N_{H_2O}=\frac{i^{S,a}_{e\text{-}O^{2-},TPB}}{2F}$ | $-n\cdot N_{O_2}=\frac{-i^{S,c}_{e\text{-}O^{2-},TPB}}{4F}$<br>$-n\cdot N_{N_2}=0$ | Continuity | $c^0_{O_2}$ $c^0_{N_2}$ |

unit dense electrolyte surface area based on the percolated LSCF-electrolyte interface can be expressed as

$$i^{S}_{e\text{-}O^{2-}}=j_{TPB}\lambda^{S}_{TPB.eff}\ (A\,m^{-2}) \tag{23}$$

where $\lambda^{S}_{TPB.eff}$ is the percolated TPB lengths per unit electrolyte surface area ($m^{-1}$) and is evaluated using electrode microstructure parameters.

For the cathode current collector with pure LSCF, only the $e^-$-$O^{2-}$ charge transfer rate per unit volume $i^{V,c}_{e\text{-}O^{2-},LSCF}$ (A $m^{-3}$) based on the percolated LSCF-pore DPBs should be considered. For Cell A, however, the charge transfer rate at the pure LSCF-cathode/electrolyte interface should also be considered, because of the absence of the LSCF-SDC cathode interlayer.

For the Ni-SDC composite anode, the $e^-$-$O^{2-}$ charge transfer rate per unit volume $i^{V,a}_{e\text{-}O^{2-},TPB}$ (A $m^{-3}$) based on the percolated Ni-SDC-pore TPB lengths per volume $\lambda^{V}_{TPB.eff}$, and the charge transfer rate at the anode/electrolyte interface $i^{S,a}_{e\text{-}O^{2-},TPB}$ can be analogously estimated by Eqs. 21 and 23, respectively. As the thickness of anode interlayer is only 6 $\mu$m, EAS may extend from the dense electrolyte surface, through the anode interlayer, to the anode support layer. Therefore, the charge transfer sources are added for the entire composite anode.

In this article, variables $I$, $j$, $i$, and $i^V$ are used to represent the electric current in A, the produced/consumed electric current per length in A $m^{-1}$, the current densities in A $m^{-2}$, and the produced/consumed electric current per volume in A $m^{-3}$.

The Dusty Gas model is thought to be sufficiently accurate to describe the multicomponent gas transport in a porous medium. For binary gas transport, the Dust Gas model can be expressed as

$$\nabla\cdot N_\alpha=R_\alpha$$
$$\frac{N_\alpha}{D^{eff}_{Kn,\alpha}}+\sum_{\beta\neq\alpha}\frac{x_\beta N_\alpha-x_\alpha N_\beta}{D^{eff}_{\alpha,\beta}}=-\frac{1}{RT}\left(p\nabla x_\alpha+x_\alpha\nabla p+\frac{x_\alpha B_0 p}{\mu D^{eff}_{Kn,\alpha}}\nabla p\right) \tag{24}$$

where $\alpha$ and $\beta$ specify two different types of gases within the porous electrode. $N_\alpha$ and $x_\alpha$ are the molar flux and molar fraction of species $\alpha$, respectively. $B_0$ is the permittivity, $\mu$ is the viscosity of the mixture, and $p$ is the total local gas pressure. According to the charge transfer rates, the species sources/leaks $R_\alpha$ (mol $m^{-3}$ $s^{-1}$) for $O_2$, $N_2$, $H_2$, and $H_2O$ in different component layers are obtained as

$$R_{O_2}=\begin{cases}-(i^{V,c}_{e\text{-}O^{2-},LSCF}+i^{V,c}_{e\text{-}O^{2-},TPB})/(4F) & \text{cathode interlayer}\\ -i^{V,c}_{e\text{-}O^{2-},LSCF}/(4F) & \text{cathode current collector}\end{cases},\qquad R_{N_2}=0\quad \text{in cathode} \tag{25}$$

$$\left.\begin{aligned}R_{H_2}&=-i^{V,a}_{e\text{-}O^{2-},TPB}/(2F)\\ R_{H_2O}&=i^{V,a}_{e\text{-}O^{2-},TPB}/(2F)\end{aligned}\right\}\ \text{in composite anode} \tag{26}$$

The effective binary diffusivities can be estimated as[25]

$$D^{eff}_{\alpha,\beta}=\frac{\phi_g}{\tau}\frac{3.24\times10^{-8}T^{1.75}}{p\left(v_\alpha^{1/3}+v_\beta^{1/3}\right)^2}\left(\frac{1}{M_\alpha}+\frac{1}{M_\beta}\right)^{0.5}\ (m^2\,s^{-1}) \tag{27}$$

where $v_\alpha$ is the diffusion volume for species $\alpha$ ($v_\alpha=6.12\times10^{-6}$, $13.1\times10^{-6}$, $16.3\times10^{-6}$, and $18.5\times10^{-6}$ $m^3$ $mol^{-1}$ for $H_2$, $H_2O$, $O_2$, and $N_2$, respectively[33]), $\phi_g$ is the porosity, $\tau$ is the tortuosity of the gas path, and $M_\alpha$ is the mole mass of species $\alpha$.

While the pore size is small compared with the mean free path of the gas molecules, gas molecules collide more frequently with the pore walls than with the other molecules. In this case, Knudsen diffusion in the porous electrode is important; and can be represented by

$$D^{eff}_{Kn,\alpha}=\frac{\phi_g}{\tau}\frac{2r_g}{3}\sqrt{\frac{8RT}{\pi M_\alpha}}\ (m^2\,s^{-1}) \tag{28}$$

where $r_g$ is the mean hydraulic pore radius.

The boundary conditions required for all interfaces (as indicated in Figure 4) are analyzed and collected in Table 4. Boundaries B1, B2, B3, B4, B5, and B6 represent the interfaces between the anode interconnect, anode support, anode interlayer, dense SDC electrolyte, LSCF-SDC composite cathode layer, pure LSCF cathode layer, and cathode interconnect, respectively. $c^0_{H_2}$, $c^0_{H_2O}$ and $c^0_{O_2}$, $c^0_{N_2}$ are the reactant concentrations at the anode and cathode channels, respectively. According to the constraint relationship between the overpotential expression and the electric boundary conditions in Assumption 4 of Table 1, the output voltage $V_{op}$ and reference voltage (0 in our case) are added at the cathode/interconnect interface B6

and anode/interconnect interface B1, respectively. The $e^-/O^{2-}$ charges sources/leaks over the anode/dense electrolyte and cathode/dense electrolyte interfaces (labeled as B3 and B4) are also considered. $i^{S,a}_{e\text{-}O^{2-},TPB}$ and $i^{S,c}_{e\text{-}O^{2-},TPB}$ (A $m^{-2}$) are the $e^-$-$O^{2-}$ charge transfer rates based on the percolated TPBs over the dense electrolyte surface $\lambda^S_{TPB,eff}$. The relevant species sources/leaks over B3 and B4 are considered by $-n\cdot N_{H_2}=-i^{S,a}_{e\text{-}O^{2-},TPB}/(2F)$, $-n\cdot N_{H_2O}=i^{S,a}_{e\text{-}O^{2-},TPB}/(2F)$, $-n\cdot N_{O_2}=-i^{S,c}_{e\text{-}O^{2-},TPB}/(4F)$, and $-n\cdot N_{N_2}=0$. For Cell A, which has a 40 $\mu$m pure LSCF cathode, B5 absent, and B4 is the interface between the pure LSCF cathode layer and the dense electrolyte layer. For Cell E which has 40 $\mu$m LSCF-SDC composite cathode, however, B5 is absent.

Generally, solving the above single cell model requires a set of electrode characteristics properties for each of the SOFC component layers, such as $\sigma^{eff}_e$, $\sigma^{eff}_{O^{2-}}$, $\lambda^V_{TPB.eff}$, $S_{es,LSCF}$, $\lambda^S_{TPB.eff}$, and $r_g$. The ability to provide the effective electrode properties of each component layer based on the material composition, microstructure parameters, and working conditions is one of the most important factors for the use of the IT-SOFC multiscale models. It is essential to further investigate and optimize the effects of the microstructure parameters and cell designs on the SOFC performance.

### *Generalized percolation micromodel for IT-SOFC composite electrode*

In our previous paper,[34] the empirical expressions for the coordination number, proposed by Suzuki and Oshima[35] were revised to satisfy the contact number conservation principle; the percolation micromodel, reported by Costamagna et al.,[36] was generalized to predict the effective properties for a conventional composite electrode with three-component random packed system (e.g., LSM-, coarse, and fine YSZ-particles).[34] In past years, the model has been widely used to evaluate the electrode properties for a conventional composite electrode that consists of pure ionic (e.g., YSZ and SDC) and electronic conducting materials (e.g., Ni and LSM). In this article, this model is adopted to calculate the electrode properties for Ni-SDC composite anode.

IT-SOFCs with electrodes that contain mixed conducting material usually show very different relationships between the microstructure parameters and macroscopic electrode characteristics than do the conventional electrodes, the generalized percolation micromodel is used to estimate the characteristic properties of LSCF-SDC composite (or pure LSCF) cathode layer from the electrode composition, microstructure parameters, and working conditions. These microstructure parameters include the volume fraction, mean particle radii, size distributions, and intrinsic properties of each material, the porosity, and working conditions. Some of these effective characteristic properties are obtained through the equations presented below

a. *The percolated LSCF-SDC-pore TPBs per unit volume*: As illustrated in Figure 1a, the percolated LSCF-SDC-pores TPBs in the porous cathode are one of alternative PEASs. It can be estimated as a function of the electrode composition and microstructure parameters

$$\lambda^V_{TPB,eff}=\gamma_{LSCF,SDC}n^V_{LSCF}Z_{LSCF,\ SDC}P^e_{LSCF}P^i_{SDC}\ (m^{-2}) \quad (29)$$

where $\gamma_{LSCF,SDC}=2\pi r_c$ is the 1-D circular length per contact between LSCF- and SDC-particles. This can be observed from an enlarged picture of Figure 1a. The neck radius depends on the smaller particle radius and the contact angle $\theta$ following $r_c=\min(r_{LSCF},r_{SDC})\sin\theta$.

$n^V_{LSCF}Z_{LSCF,\ SDC}$ is the number of LSCF-SDC contact points per unit electrode volume. The number of $k$-particles per unit volume in the entire cathode structure can be estimated as $n^V_k=(1-\phi_g)\psi_k/[4\pi r_k^3/3]$. $\psi_k$ is the solid volume fraction of $k$-particles. $Z_{LSCF,SDC}$ is the average number of contacts between the LSCF-particle and all of its neighboring SDC-particles. It can be estimated through the revised coordination number expression as[34]

$$Z_{k,\ell}=0.5(1+r_k^2/r_\ell^2)\bar{Z}\frac{\psi_\ell/r_\ell}{\sum_{k=1}^{M}\psi_k/r_k} \quad (30)$$

where $\bar{Z}=6$ is the average coordination number of all of the particles in a random close packing of rigid spherical particles.[37] Compared with the expressions reported by Suzuki and Oshima,[35] Eq. 30 proved to be better able to satisfy the contact number conservation principle $n^V_k Z_{k,\ell}=n^V_\ell Z_{\ell,k}$.

$P^i_{LSCF}$ and $P^e_{LSCF}$ are defined as the probabilities that the LSCF-particles belong to the percolated ionic and electronic conduction paths, respectively; $P^i_{SDC}$ is the probability that the SDC-particles belong to the percolated ionic conduction path. For the LSCF-SDC composite cathode, $P^i_{LSCF}=P^i_{SDC}=1$, and $P^e_{LSCF}$ can be estimated as[38,39]

$$P^e_{LSCF}=1-\left(\frac{4.236-Z_{LSCF,\ LSCF}}{2.472}\right)^{3.7} \quad (31)$$

b. *The percolated LSCF-pore DPBs per unit volume*: As shown in Figure 1c, the percolated LSCF-pore DPBs per electrode volume are considered to be another important type of PEAS for the cathode $e^-$-$O^{2-}$ charge transfer reaction. This is proportional to the number of LSCF-particles per unit volume $n^V_{LSCF}$, the exposed surface area of each LSCF-particle $s_{es}$ and the probabilities that the LSCF-particles belong to both the percolated electronic and ionic conducting paths $P^e_{LSCF}P^i_{LSCF}$[40]

$$S_{es,LSCF}=n^V_{LSCF}s_{es}P^e_{LSCF}P^i_{LSCF}\ (m^{-1}) \quad (32)$$

As observed from an enlarge picture of Figure 1c, $s_{es}$ can be determined by subtracting the overlap between the neighboring particles from the spherical surface area of the percolated LSCF-particle, as given by

$$s_{es}=2\pi r^2_{LSCF}[2-(1-\cos\theta_{LSCF})Z_{LSCF,\ LSCF}-(1-\cos\theta_{LSCF})Z_{LSCF,\ SDC}]\ (m^{-1}) \quad (33)$$

The contact angles $\theta_{LSCF}$ between $r_{LSCF}$- and its neighboring $r_2$-particles should satisfy the relationship $r_{LSCF}\sin\theta_{LSCF}=r_2\sin\theta_2$.[40]

c. *The percolated TPBs per unit dense electrolyte surface area*: The percolate TPBs over the dense electrolyte surface are also important PEAS for the $e^-$-$O^{2-}$ charge transfer reaction.[29] The percolated TPBs per unit electrolyte surface area can be estimated by

$$\lambda^S_{TPB,eff}=\gamma_{LSCF,ele}\,n^S_{LSCF}P^e_{LSCF}\ (m^{-1}) \quad (34)$$

where the 1-D circular length per contact between LSCF-particle and the dense electrolyte surface can be evaluated as $\gamma_{LSCF,ele}=2\pi r_{LSCF}\sin\theta$ (shown in Figure 1b). The number of LSCF-particles per unit dense electrolyte surface can be calculated as $n^S_{LSCF}=(1-\phi_g)\psi_{LSCF}/(2\pi r^2_{LSCF}/3)$.[29,34]

d. *The effective ionic and electronic conductivities*: The intraparticle and interparticle electric conductivities represent the charge transport capabilities through the interiors of the

particles and through the particle-particle interfaces, respectively. For an LSCF-SDC composite cathode, both the LSCF- and SDC-particles contribute to the $O^{2-}$ conduction path. It is acceptable to assume that the ionic intraparticle conduction paths of LSCF- and SDC-particles within each particle layer are connected in parallel, such that there are three parallel paths (i.e., LSCF-LSCF, SDC-SDC, and LSCF-SDC interfaces) available for $O^{2-}$ transport through the particle layer interfaces.[37,40] This is described by

$$\sigma_{O^{2-}}^{\text{eff}} = \left( \frac{1}{\sigma_{\text{SDC}}^{\text{i,tra,eff}} + \sigma_{\text{LSCF}}^{\text{i,tra,eff}}} + \frac{1}{\sigma_{\text{SDC-SDC}}^{\text{i,ter,eff}} + \sigma_{\text{LSCF-LSCF}}^{\text{i,ter,eff}} + \sigma_{\text{LSCF-SDC}}^{\text{i,ter,eff}}} \right)^{-1} (\text{S m}^{-1}) \tag{35}$$

where $\sigma_{mat}^{\text{i,tra,eff}}$ is the effective ionic intraparticle conductivity of *mat*-material based on the electrode geometry. It can be simply estimated as[25,41]

$$\sigma_{mat}^{\text{i,tra,eff}} = \sigma_{mat}^{\text{i,tra,0}} \left( \psi_{mat} (1 - \phi_{\text{g}}) \right)^2 (\text{S m}^{-1}) \tag{36}$$

where $\sigma_{mat}^{\text{i,tra,0}}$ is the intrinsic ionic intraparticle conductivity of *mat*-material in a dense solid.

$\sigma_{k-l}^{\text{i,ter,eff}}$ is the effective interparticle ionic conductivities among the ionic conductors, such as LSCF-LSCF, SDC-SDC, and LSCF-SDC. Careful analysis of the results shows that $\sigma_{k-l}^{\text{i,ter,eff}}$ should be evaluated based on the smaller particle layer $2\min(r_k, r_l)$.[40] The empirical expression for $\sigma_{k-l}^{\text{i,ter,eff}}$, reported by Chan,[37] should then be generalized and revised as

$$\sigma_{k-l}^{\text{i,ter,eff}} = \sigma_{k-l}^{\text{i,ter,0}} \frac{4 a_{k-l} \min(r_k, r_l)^2 n_k^{\text{V}} Z_{k,l} P_k^{\text{i}} P_l^{\text{i}}}{\delta_{k-l}} (\text{S m}^{-1}) \tag{37}$$

where $\delta_{k-l}$ is the interface thickness between *k*- and *l*-particles, which is estimated to be approximately 5 nm.[42] $a_{k-l} = \pi r_{\text{c}}^2$ is the per contact area between *k*- and *l*-particles. $\sigma_{k-l}^{\text{i,ter,0}}$ is the intrinsic ionic interparticle conductivity.

As the interparticle electronic conductivity is sufficiently large making a negligible contribution to resistance to the total electronic conduction, a definition that is analogous to Eq. 36 is used to evaluate the effective electronic conductivity $\sigma_{\text{e}}^{\text{eff}}$ based on the geometry.

e. *The hydraulic radius of the porous cathode structure*: This is an important factor for the determination of the multicomponent gas transport in the porous media; and can be calculated as[34]

$$r_{\text{g}} = \frac{2}{3} \left( \frac{\phi_{\text{g}}}{(1 - \phi_{\text{g}})} \right) \left( \frac{\psi_{\text{LSCF}}}{r_{\text{LSCF}}} + \frac{\psi_{\text{SDC}}}{r_{\text{SDC}}} \right)^{-1} (\text{m}) \tag{38}$$

The intrinsic electric conductivities of each material are required to use the generalized percolation micromodel to evaluate the effective characteristic properties of each IT-SOFC component from the electrode composition, microstructure parameters, and operating conditions. As most of the experiment values for these properties had been measured at various temperatures, many convenient formulas achieved by fitting the reported experimental data are presented in Supporting Information.

## Results and Discussion

### *Multiscale models verification*

The finite element commercial software COMSOL Multiphysics is used in the present study to solve the coupled partial differential equations of electronic, ionic, and gas transports. The source (or leak) items within the single cell model are modeled using the mathematical relations presented in the macromodel section. The boundary conditions required to simulate the five different IT-SOFCs are listed in Table 4; here, Assumptions 4 of Table 1 is adopted to describe the constraint relationship between the overpotential expressions and electric boundaries. The effective characteristic properties of each component layer are calculated through the generalized (or traditional) percolation micromodel and the fitting formulas of intrinsic properties for each material.

**Table 5. The Working Conditions and Parameters for the Modeling**

| Parameters | Value |
|---|---|
| $E_{O_2}$ (J mol$^{-1}$) | $130 \times 10^3$, Ref. 28 |
| $\alpha_{\text{LSCF}}^{\text{c}}$, $\beta_{\text{LSCF}}^{\text{c}}$ | 0.5, 0.5 |
| $i_{\text{LSCF,ref}}$ (A m$^{-2}$) | $3.0 \times 10^4$ |
| $\alpha_{\text{f}}^{\text{c}}$,$\beta_{\text{r}}^{\text{c}}$ | 0.5, 0.5 |
| $j_{0,\text{ref}}^{\text{c}}$ (A m$^{-1}$) | $1 \times 10^{-5}$ |
| $E_{H_2}$ (J mol$^{-1}$) | $120 \times 10^3$, Ref. 27,28 |
| $\alpha_{\text{f}}^{\text{a}}$, $\beta_{\text{r}}^{\text{a}}$ | 1, 0.5, Ref. 27,28 |
| $j_{0,\text{ref}}^{\text{a}}$ (A m$^{-1}$) | $8.0 \times 10^{-2}$ |
| *ad* | 0.7 |
| $p_{H_2}^0$, $p_{H_2O}^0$ (atm) | 0.97, 0.03 |
| $p_{O_2}^0$, $p_{N_2}^0$ (atm) | 0.21, 0.79 |

Most of the electrode composition, microstructure parameters, and operating temperature are obtained from the experiment data, reported by Wang et al.,[14] which allows our model to correspond to the experimental data as much as possible. Table 3 lists the basic model parameters with the experimental sources specified. Assuming that all of the particles within the composite electrode are spheres, the material volume ratios within each material layer are estimated using the particle diameters, mass ratios, and specific areas reported in the literature.[14] Based on the percolation micromodels for LSCF-SDC (or Ni-SDC) composite electrode, the effective electrode properties of each component layer, such as $\lambda_{\text{TPB,eff}}^{\text{V}}$, $S_{\text{es,LSCF}}$, $\lambda_{\text{TPB,eff}}^{\text{S}}$, $\sigma_{\text{e}}^{\text{eff}}$, $\sigma_{O^{2-}}^{\text{eff}}$, and $r_{\text{g}}$ are calculated from the reported parameters, and the calculated results are collected in Table 3.

The calculated result in Table 3 shows that the pure LSCF layer and LSCF-SDC composite layer exhibit very different characteristics. Compared with the pure LSCF cathode, the use of the LSCF-SDC composite cathode introduces additional percolated LSCF-SDC-pore TPBs per unit volume $\lambda_{\text{TPB,eff}}^{\text{V}} = 3.62 \times 10^{12}$ m$^{-2}$ and increase the total effective ionic conductivity of the cathode structure (i.e., $\sigma_{O^{2-}}^{\text{eff}}$ increases from 0.068 to 0.104 S m$^{-1}$ at 600°C), because of the higher intrinsic $O^{2-}$ conductivity of the SDC-material. At the same time, the increased SDC-loading also leads to a lower $\sigma_{\text{e}}^{\text{eff}}$ (i.e., decrease from $4.82 \times 10^4$ to $2.03 \times 10^4$ S m$^{-1}$ at 600°C) and decreases both the percolated volume LSCF-pore DPBs $S_{\text{es,LSCF}}$ from $2.02 \times 10^6$ to $1.29 \times 10^6$ m$^{-1}$ and the percolated TPBs over the dense electrolyte surface $\lambda_{\text{TPB,eff}}^{\text{S}}$ from $1.63 \times 10^6$ to $9.13 \times 10^5$ m$^{-1}$.

As several parameters could not be obtained directly from experiments or the literatures, they should be obtained by tuning the model. Generally, a smaller number of adjustable parameters and a larger size of the experiment fitting database are favorable for higher reliability of the developed theory models. In Eqs. 8, 12, and 14, $j_{\text{TPB,0,ref}}^{\text{a}}$ $j_{\text{TPB,0,ref}}^{\text{c}}$, and $i_{\text{LSCF,0,ref}}$ at the reference temperature $T_{\text{ref}} = 800$°C and $\alpha_{\text{f}}^{\text{c}}$ and $\alpha_{\text{LSCF}}^{\text{c}}$ in Eqs. 7 and 13 are the only parameters that had to be adjusted to fit the reported 25 *I-V* experimental curves. The factor *ad*

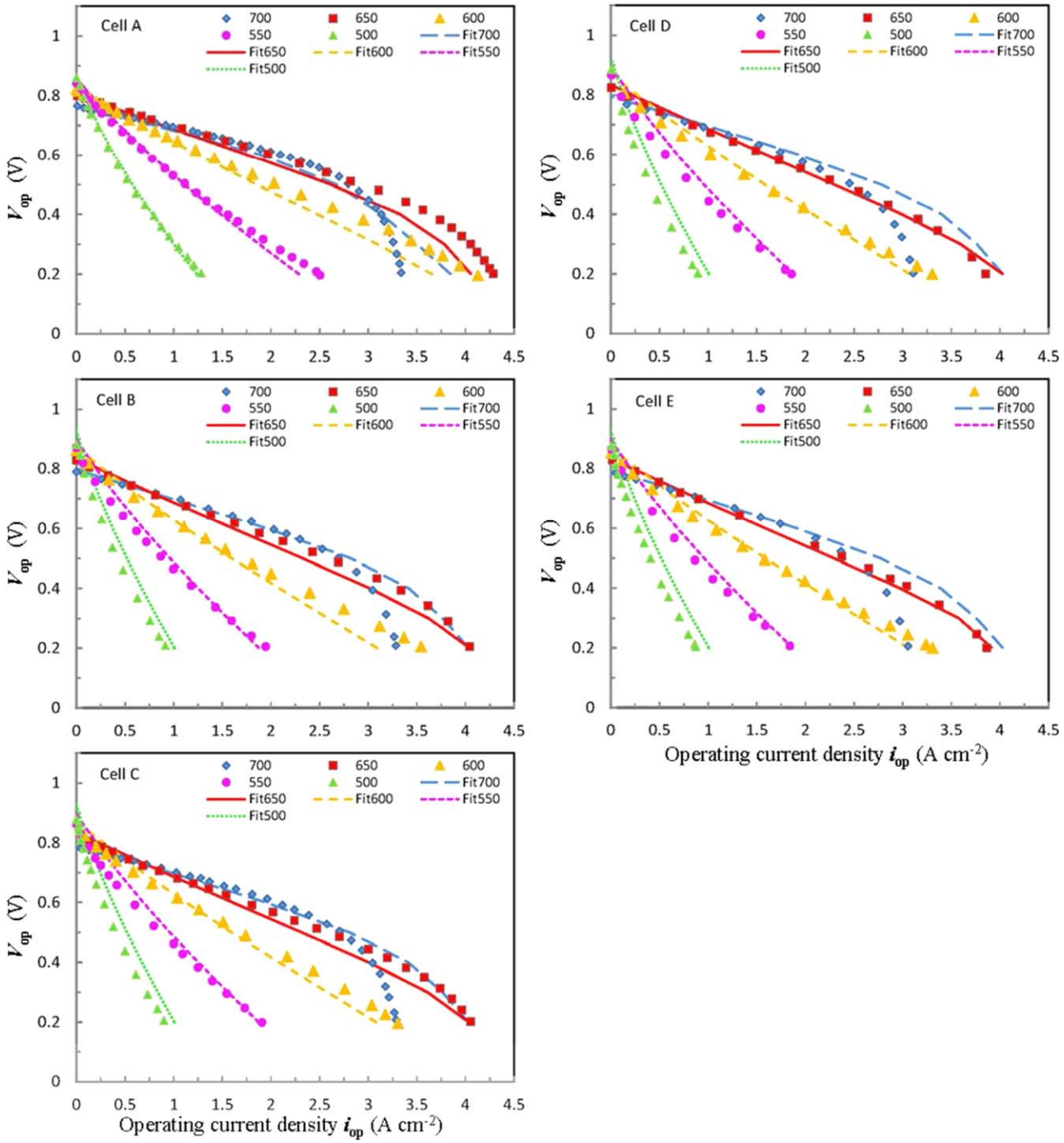


**Figure 5. The reported experimental *I-V* curves from five different IT-SOFCs at various *T* are fitted with few adjustable parameters all at once, (a) Cell A; (b) Cell B; (c) Cell C; (d) Cell D; (e) Cell E.**

**[Color figure can be viewed in the online issue, which is available at wileyonlinelibrary.com.]**

for the LSCF-SDC composite electrode is added to the electronic/ionic electric conductivities of the dense electrolyte to represent the effects of the additional interface contact resistance among different component layers and the LSCF-SDC interparticle resistance for the $O^{2-}$ conducting in composite electrode.[14] The operating condition are $p^0_{H_2}=0.97$, $p^0_{H_2O}=0.03$, $p^0_{O_2}=0.21$, and $p^0_{N_2}=0.79$ atm. All of the parameters used in the modeling are collected in Table 5.

Based on the electrode characteristics presented in Table 3 and the parameters presented in Table 5, all of the 25 literature experimental *I-V* curves at various temperatures (i.e., 500, 550, 600, 650, and 700°C) from five different cells (shown in Table 2)[14] are fitted with only a few adjustable parameters. As shown in Figures 5a–e, good agreement between the theoretical and 25 experiment *I-V* curves is achieved, which demonstrates the validity of the generalized multiscale SOFC models described above.

### *Comparison of the pure LSCF and LSCF-SDC composite cathodes*

Both the experimental and model results presented in Figures 5a–e show that the cell performances decrease with increased LSCF-SDC composite cathode thickness; the

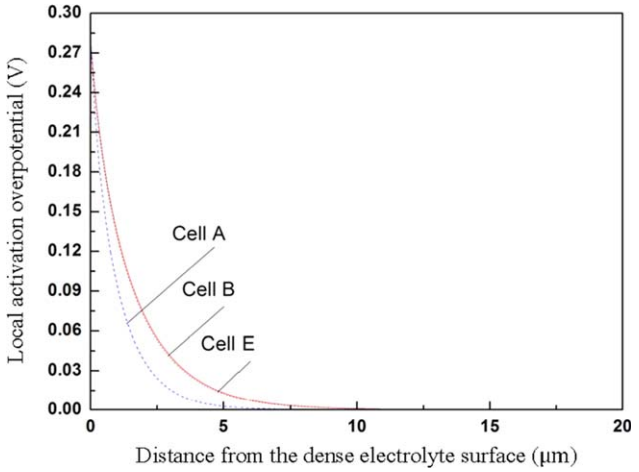


**Figure 6. The local $\eta^{c}_{lact}$ distribution within the cathode as a function of the distance away from the dense electrolyte surface.**

**[Color figure can be viewed in the online issue, which is available at wileyonlinelibrary.com.]**

performances are in the order, Cell A > Cell B ≥ Cell C ≥ Cell D ≥ Cell E, with Cells B, C, D, and E showing quite similar performances. Obviously, although the use of the LSCF-SDC composite cathode can increase $\lambda^{V}_{TPB.eff}$ and $\sigma^{eff}_{O^{2-}}$ in comparison with the pure LSCF cathode layer, it does not lead to a large enhancement of the cell performance. This phenomenon is very different from the conventional SOFCs with composite electrodes that consist of the pure electronic and ionic conductors (i.e., LSM-YSZ), in which increasing $\lambda^{V}_{TPB.eff}$ and $\sigma^{eff}_{O^{2-}}$ greatly reduces the cathode activation polarization and improve the cell performance. The small improvement obtained here may be attributed to the following factors

i. the most important reason is that increasing the SDC-loading greatly reduces both $S_{es,LSCF}$ from $2.02 \times 10^6$ to $1.29 \times 10^6$ $m^{-1}$ and $\lambda^{S}_{TPB,eff}$ from $1.63 \times 10^6$ to $9.13 \times 10^5$ $m^{-1}$ (shown in Table 3). As illustrated above, $\lambda^{V}_{TPB.eff}$, $S_{es,LSCF}$, $\lambda^{S}_{TPB,eff}$ are three important PEAS types for LSCF-SDC composite cathode. Which and how many part of them can be EAS, should further depend on the details of electron, ion, and species transport capabilities and electrochemical activities around these PEASs. Taking Cell E at $T = 600°C$ and $i_{op} = 2.5 \times 10^4$ A $m^{-2}$ operating condition as an example, the modeling result shows that the cathode $e^{-}$-$O^{2-}$ charge transfer rate produced by the percolated volume LSCF-SDC-pore TPBs represents less than 5% of the total amount. Most of the $e^{-}$-$O^{2-}$ charge transfer reactions are supported by the percolated TPBs over the dense electrolyte surface because of the very short ionic conducting path and the percolated volume LSCF-SDC DPBs. Thus, unlike the case of LSCF coated with SDC,[13] for LSCF-SDC composite cathodes, the oxygen reduction activities around the percolated volume LSCF-SDC-pores TPBs are smaller than the percolated LSCF-pore DPBs. A similar conclusion for composite LSCF-CGO had also be obtained by experiment reported by Esquirol et al.[43] This conclusion can also be supported by the X-ray diffraction reported by Wang et al.,[14] which shown that there were not chemical change at the LSCF-SDC interfaces.

ii. although the increased the SDC-loading dose increase $\sigma^{eff}_{O^{2-}}$ from 0.068 to 0.104 S $m^{-1}$ at 600°C (listed in Table 3), the $O^{2-}$ transport may suffer from the large LSCF-SDC interparticle resistance before it can use the high ionic conductivity of the SDC-conductor. Because most of the oxygen reduction reactions in the cathode body take place around the percolated LSCF-pore DPBs and located over the LSCF side, as described in factor (i);

iii. as shown in Table 3, the electronic conducting capability $\sigma^{eff}_{e}$ decreases by more than 50% from the pure LSCF cathode to the LSCF-SDC composite cathode. This greatly decreases the overall electric conductivity of the entire cathode layer, because of the larger electronic conductivity value relative to the ionic conductivity. This behavior is consistent with the experimental results reported by Wang et al.[14] and Yu et al.[44]

### *Thickness of the real EAS*

Although the percolated LSCF-pore DPBs have been found to be the dominant sites to support the cathode electrochemical reactions in comparison with the percolated LSCF-SDC-pore TPBs, only a fraction of these sites can be EAS. As shown in Figure 6, for Cell E, the EAS extends 10 $\mu$m from the dense electrolyte surface into the composite cathode, and the remaining cathode structure is inactive. This conclusion is further supported by the reported experimental results shown in

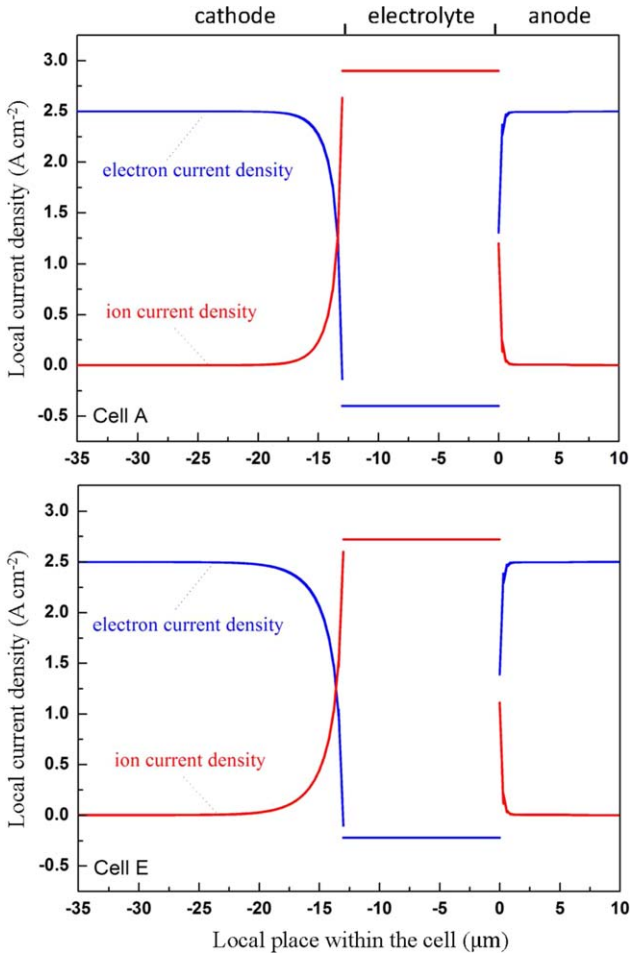


**Figure 7. Distributions of both $i_e$ and $i_{O^{2-}}$ within IT-SOFCs at $T = 600°C$ and $i_{op} = 2.5 \times 10^4$ A $m^{-2}$.**

**Discontinuities of the $i_e$ and $i_{O^{2-}}$ distributions at the electrode/dense electrolyte interfaces indicate the charge transfer rates by $\lambda^{S}_{TPB}$. (a) Cell A; (b) Cell E. [Color figure can be viewed in the online issue, which is available at wileyonlinelibrary.com.]**

**Table 6. The Theory Standard Nernst Potentials, Ideal Theory OCVs, and the Simulated Real OCVs for Five IT-SOFCs at Various *T***

| | LSCF/LSCF-SDC | 500°C | 550°C | 600°C | 650°C | 700°C |
|---|---|---|---|---|---|---|
| NP at standard | | 1.06 V | 1.05 V | 1.04 V | 1.02 V | 1.01 V |
| Theory OCV 1 | | 1.15 V | 1.15 V | 1.14 V | 1.13 V | 1.12 V |
| Theory OCV 2 | | 1.08 V | 1.07 V | 1.06 V | 1.05 V | 1.03 V |
| OCV of Cell A | 40 $\mu$m/0 $\mu$m | 0.87 V | 0.86 V | 0.83 V | 0.80 V | 0.77 V |
| OCV in Cell B | 30 $\mu$m/10 $\mu$m | 0.92 V | 0.88 V | 0.87 V | 0.83 V | 0.79 V |
| OCV of Cell C | 20 $\mu$m/20 $\mu$m | 0.92 V | 0.89 V | 0.87 V | 0.83 V | 0.79 V |
| OCV of Cell D | 10 $\mu$m/30 $\mu$m | 0.92 V | 0.89 V | 0.87 V | 0.83 V | 0.79 V |
| OCV of Cell E | 0 $\mu$m/40 $\mu$m | 0.92 V | 0.89 V | 0.87 V | 0.84 V | 0.79 V |

Note: Theory OCV 1 and OCV 2 indicated the calculated ideal Nernst potentials at $p^0_{H_2}/p^0_{O_2} = 0.97/0.21$ and 0.8/0.21, respectively.

Figures 5b–e.[14] Although the LSCF-SDC composite and pure LSCF cathode layers exhibit very different properties and Cells B–E have different thickness combinations (listed in Table 2), similar *I-V* curves were obtained for Cells B, C, D, and E whose the LSCF-SDC composite layer thicknesses were larger than 10 $\mu$m. It means that 10-$\mu$m LSCF-SDC composite cathode thickness is sufficient to support most of the cathode electrochemical reaction; and that the effect of the cathode structure beyond this thickness on the cathode activation polarization is relatively small.

Furthermore, Figure 6 shows that the extended EAS thickness within Cell E with a 40-$\mu$m LSCF-SDC composite cathode is larger than that within Cell A with a 40-$\mu$m pure LSCF cathode. This difference is due to the lower percolated LSCF-pore DPBs $S_{es,LSCF}$ and higher $O^{2-}$ conducting capability $\sigma^{eff}_{O^{2-}}$ in Cell E than that in Cell A. As discussed above, a higher $\sigma^{eff}_{O^{2-}}$ means that $O^{2-}$ can be transported farther away from the dense electrolyte surface with a lower potential drop. It can also extend the thickness of the EAS and reduce the $\eta^c_{act}$; additionally, a lower $S_{es,LSCF}$ means that a more electrochemical active zone and a higher $\eta^c_{act}$ distribution are required for the charge transfer reactions, while the output current density is fixed. Therefore, both of these two factors contribute to a larger EAS thickness in Cell E. Thus, we can conclude that, for IT-SOFCs using LSCF-material, a 10 $\mu$m cathode thickness is sufficient to support most of the cathode electrochemical reactions.

Figure 7 shows the distributions of both the electronic (blue points) and ionic (red points) electric current densities ($i_e$ and $i_{O^{2-}}$) in Cells A and E at $T = 600$°C and $i_{op} = 2.5 \times 10^4$ A m$^{-2}$. The cathode zone extends from $-35$ to $-13$ $\mu$m, the dense electrolyte is from $-13$ to 0 $\mu$m, and the anode zone goes from 0 to 10 $\mu$m. Discontinuities of the $i_e$ and $i_{O^{2-}}$ distributions at the electrode/dense electrolyte interfaces indicate the amount of current density conversions by the percolated TPBs over the dense electrolyte surfaces. It is obvious that only a limited thickness of the cathode involved in the electrochemical charge transfer reaction between $i_e$ and $i_{O^{2-}}$, with the rest of the cathode remaining electrochemically inactive. Although the SDC-material may exhibit a high $\sigma^{eff}_{O^{2-}}$ at the IT working regime, the $e^-$ conducting capability within the dense SDC electrolyte cannot be ignored.

As observed from Figure 7a for Cell A, within the cathode reaction zone, the $i_e$ is gradually converted into $i_{O^{2-}}$. The amplitude of $i_e$ on the electrode zone is $i_e = 2.5 \times 10^4$ A m$^{-2}$; that equals to the output current density $i_{op} = 2.5 \times 10^4$ A m$^{-2}$. However, a larger amplitude of $i_{O^{2-}} = 2.9 \times 10^4$ A m$^{-2}$ is achieved in the dense electrolyte zone compared with $i_{op}$. The positive values of $i_e$ and $i_{O^{2-}}$ within the electrodes indicate that most of the $i_e$ and $i_{op}$ flow along the $y$ direction from the anode side through the dense electrolyte to the cathode side (shown in Figure 3). It is necessary to note that, the $i_e$ in the entire dense electrolyte and part of the cathode reaction zone are negative; a minimal value $i_{leak} = -0.4 \times 10^4$ A m$^{-2}$ can be achieved and kept within the dense electrolyte. These can be attributed to the $e^-$ conducting capability of the dense SDC electrolyte. Here, the negative sign represents the fact that part of the $i_e$ flows from the cathode side to the anode side through the dense electrolyte directly. Because it does not flow through the external load, it is considered to be an electronic leakage current. Thus, the amplitudes of $i_{O^{2-}}$, instead of the $i_{op} = 2.5 \times 10^4$ A m$^{-2}$, should be used to evaluate the fuel/oxygen

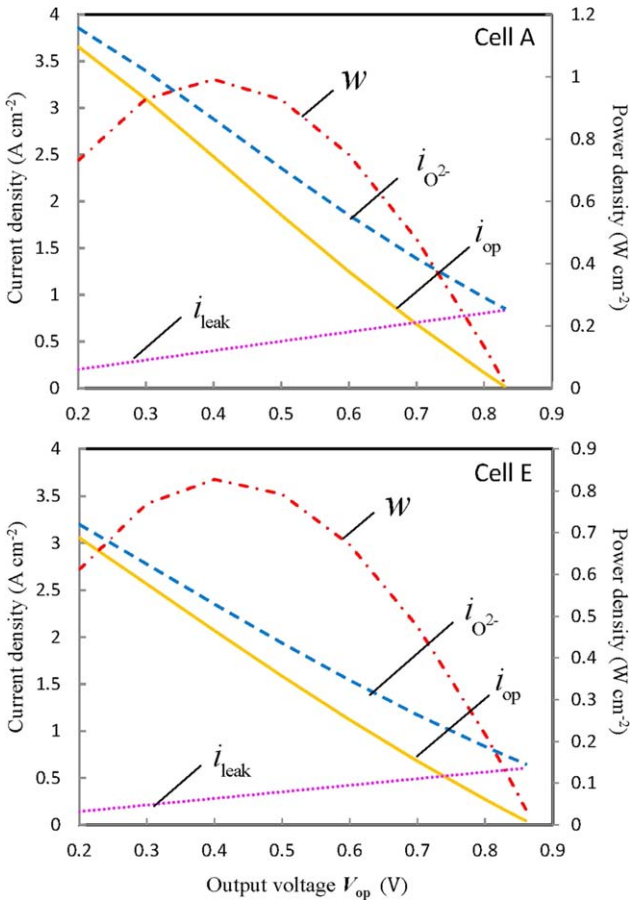


**Figure 8. The $i_{op}$, $i_{O^{2-}}$, and $i_{leak}$ through the dense electrolyte of Cell A as a function of $V_{op}$ at 600°C, $p^0_{H_2} = 0.97$, and $p^0_{O_2} = 0.21$.**

**[Color figure can be viewed in the online issue, which is available at wileyonlinelibrary.com.]**

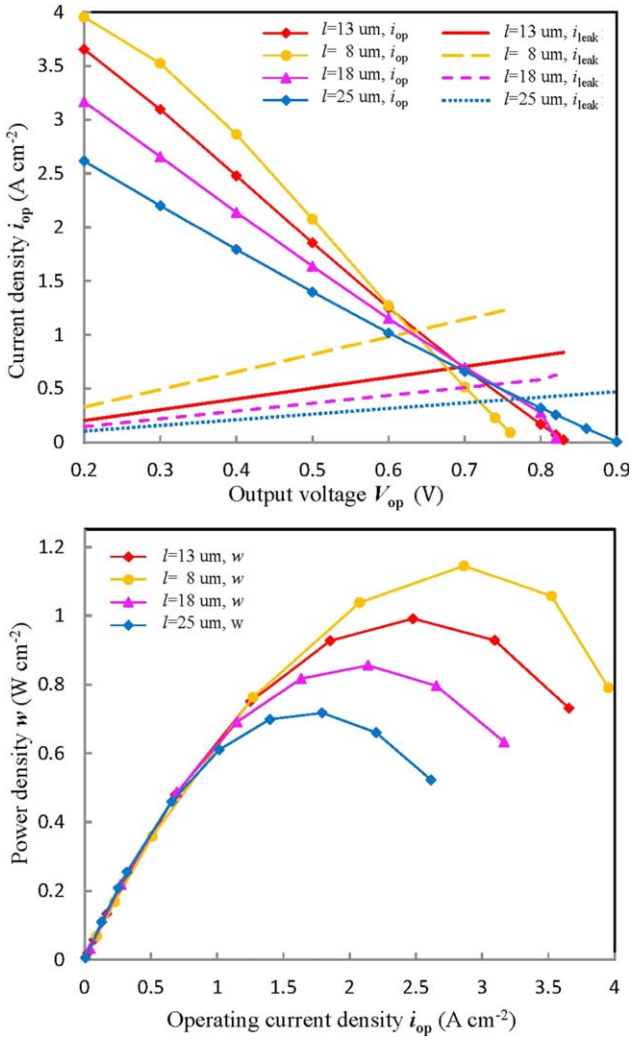


**Figure 9. (a) The effects of $V_{op}$ and dense electrolyte thickness $l$ on the $i_{op}$ and $i_{leak}$ for Cell A at $T = 600°C$; (b) the dependence of the output power density on the $i_{op}$ and $l$.**

**[Color figure can be viewed in the online issue, which is available at wileyonlinelibrary.com.]**

consumptions, and $|i_{O^{2-}}| = |i_{op}| + |i_{leak}|$. Similarly, for Cell E, the amplitudes of $i_{O^{2-}}$, $i_e$, and $i_{leak}$ at $T = 600°C$ and $i_{op} = 2.5 \times 10^4$ A m$^{-2}$ are $2.72 \times 10^4$, $2.5 \times 10^4$, and $-0.22 \times 10^4$ A m$^{-2}$, respectively. Compared with Cell A with a 40-$\mu$m pure LSCF cathode, using the LSCF-SDC composite cathodes (e.g., Cells B–E) reduces the $i_{leak}$ and increases the OCV (e.g., from 0.83 to 0.87 V at 600°C).

### *Effects of the internet electronic current leakages through dense electrolyte*

In Table 6, the standard theory Nernst potentials, ideal theory OCVs, and the simulated real OCVs for five IT-SOFCs at various $T$ are collected and compared. The standard Nernst potential, ideal theory OCV 1, and OCV 2 are calculated by the ideal Nernst potential expressions based on standard state (1 atm); and $p^0_{H_2}/p^0_{O_2} = 0.97/0.21$ and 0.8/0.21 cases, respectively. The real OCVs for Cells A–E are obtained from the modeling results in Figure 5. Good agreements between these modeled real OCVs and the experimental data, reported by Wang et al.,[14] further demonstrates the validity of the developed multiscale models. As there are internal electronic current leakages through the dense SDC-electrolyte, the real OCVs in Cells A–E are significantly decreased compared with the ideal theory OCV 1 values; these decreases in the real OCV values become more pronounced as the operating temperatures increases. Compared with Cell A with a 40-$\mu$m pure LSCF cathode, Cells B–E with LSCF-SDC composite cathodes exhibit higher OCVs, because of their relatively high gas transport and electronic conduction resistances.

Figure 8a shows the $i_{op}$ and the ionic and leakage electric current densities ($i_{O^{2-}}$ and $i_{leak}$) through the dense electrolyte of Cell A as a function of the output voltage $V_{op}$ at $T = 600°C$, $p^0_{H_2} = 0.97$, and $p^0_{O_2} = 0.21$. The calculated result shows that the produced ionic and output electric currents ($i_{O^{2-}}$ and $i_{op}$) decrease with increasing $V_{op}$. The electronic leakage current $i_{leak}$, however, increases with the increasing $V_{op}$. This means that although the dense electrolyte internal electric leaking phenomena can strongly affect the OCVs, their effect on the IT-SOFC performance in the operating regime is relatively small, especially at the high $i_{op}$ conditions (i.e., $V_{op} < 0.6$ V). This conclusion is considered to be reasonable by analyzing Figure 1: (1) the effects of internal electric leakage in the dense electrolyte stand out for the open circuit conditions, because in that case, the dense electrolyte is the only electronic conduction path from the anode to the cathode sites. Therefore, internal electric leakage has a strong impact on the OCV; (2) in contrast, when the external circuit is connected, most of the produced electrons at the anode side may choose the external conduction path; instead of the dense electrolyte; to achieve the lowest ohm potential loss from the anode side to the cathode sites. The dependence of the electron transport on the dense electrolyte will be very small. Similarly, the effects of $V_{op}$ on the $i_{op}$, $i_{O^{2-}}$ and $i_{leak}$ within the dense electrolyte of Cell E at $T = 600°C$, $p^0_{H_2} = 0.97$, and $p^0_{O_2} = 0.21$ case are shown in Figure 8b. Conclusively, although the internal electronic leaking can greatly reduce the IT-SOFC OCV and increasing the fuel/oxygen consumptions, its effects on the SOFC performance at the main operating regime are relatively small.

To further check the effect of the dense electrolyte internal electric leaking phenomena on the SOFC performance in the typical operating regime, the influence of varying the dense electrolyte thickness $l$ on the IT-SOFC performance is investigated for Cell A at $T = 600°C$. Figure 9a shows that the $i_{leak}$ greatly decreases with the increased $l$, which leads to an increase in the OCVs from 0.76 to 0.9 V for an $l$ increases from 8 to 25 $\mu$m. This result provides an additional

**Table 7. The Effects Three Different LSCF Loadings on the Effective Characteristic Properties of the LSCF-SDC Composite Layers at 600°C**

| | $\sigma_e^{eff}$ (S m$^{-1}$) | $\sigma_{O^{2-}}^{eff}$ (S m$^{-1}$) | $r_g$ ($\mu$m) | $\lambda^V_{TPB,eff}$ (m$^{-2}$) | $S_{es,LSCF}$ (m$^{-1}$) | $\lambda^S_{TPB,eff}$ (m$^{-1}$) |
|---|---|---|---|---|---|---|
| $\psi_{LSCF}=0.61$ | $1.12 \times 10^4$ | 0.1035 | 0.414 | $3.62 \times 10^{12}$ | $1.29 \times 10^6$ | $9.13 \times 10^5$ |
| $\psi_{LSCF}=0.5$ | $1.79 \times 10^3$ | 0.1390 | 0.386 | $1.73 \times 10^{12}$ | $5.24 \times 10^5$ | $3.64 \times 10^5$ |
| $\psi_{LSCF}=0.7$ | $1.99 \times 10^4$ | 0.0836 | 0.439 | $3.93 \times 10^{12}$ | $1.67 \times 10^6$ | $1.22 \times 10^6$ |

demonstration that the internal electric leakage has a strong effect on the OCV. However, the ratio of $i_{leak}/i_{op}$ decreases significantly with decreased $V_{op}$. For most of the typical operating regime (i.e., $V_{op} = 0.3$–$0.65$ V), higher $I$-$V$ performance is achieved when a thinner electrolyte layer is used. Figure 9b further shows the output power density $W$ as a function of the $i_{op}$ and various values of the electrolyte thicknesses $l$ at $T = 600$°C. It is obvious that a higher IT-SOFC performance is obtained for thinner electrolyte thickness, particularly in the high $i_{op}$ zone. While the dense electrolyte thickness is changed, the ionic ohmic polarization, in comparison with the internal electronic leakage, still plays the critical role in the IT-SOFC performance. The influences of the internal electric leakage would be restricted to the low $i_{op}$ zone around the OCVs, its effects in the IT-SOFC typical operating regime ($V_{op} = 0.3$–$0.65$ V) are quite small. These results further support the conclusion that can be drawn from Figure 8.

### *Effects of LSCF loading on the electrode properties and cell performance*

Generally, the verified multiscale model can be further used to study the effects of the electrode composition, microstructure parameters, and operating conditions on the electrode characteristic properties and the cell performances. As an example to illustrate the application, while all the other microstructure parameters are kept, the effects of three different LSCF loadings on the effective characteristic properties of LSCF-SDC composite layer and the cell performance at 600°C are calculated. The calculated electrode properties are collected in Table 7. As can be seen from Figure 10a, while $\psi_{LSCF}$ decreases from 0.61 to 0.5, the performance of Cell E will be greatly decreased. For $\psi_{LSCF}$ within the range of 0.61–0.7, however, the effects of LSCF loading on the performance of Cell E will be neglected. These results may attribute to the instinct properties of LSCF and SDC materials and large ratio of their particle sizes $r_{LSCF}/r_{SDC} = 0.99/0.55 > 1$. Figure 10b shows the relevant local activation overpotential distribution within the composite cathode $\eta^{c}_{act}$. For $\psi_{LSCF}=0.5$, the thickness of the EAS will be greatly increased, because of the increasing of $\sigma^{eff}_{O^{2-}}$ and the decreasing of $S_{es,LSCF}$, $\lambda^{S}_{TPB,eff}$, $\lambda^{V}_{TPB,eff}$, and $\sigma^{eff}_{e}$ (shown in Table 7). For $\psi_{LSCF}=0.7$, however, the thickness of the EAS will decrease slightly, because of the decreasing of $\sigma^{eff}_{O^{2-}}$ and slight increasing of $S_{es,LSCF}$, $\lambda^{S}_{TPB,eff}$, and $\lambda^{V}_{TPB,eff}$. Considering the restriction of the article length, the effects of all other compositions, microstructure parameters, geometries, and working conditions on the characteristic properties of each electrode layers, and further on the working details will be further completed in the near future to achieve the optimized guidelines.

## Conclusion

The multiscale predictive models for the typical SOFCs using mixed conducting materials are developed and validated. The developed multiscale models consist of a generalized percolation micromodel and a multiphysics single cell model, and they can be applied to provide a quantitative connection among the electrode microstructures, the effective characteristic properties of each component, and the detailed IT-SOFC performance. Taking the typical LSCF-SDC/SDC/Ni-SDC as an example, the development of the multiscale models was fully illustrated and validated using a series of experiment results obtained from literature; and the follwing

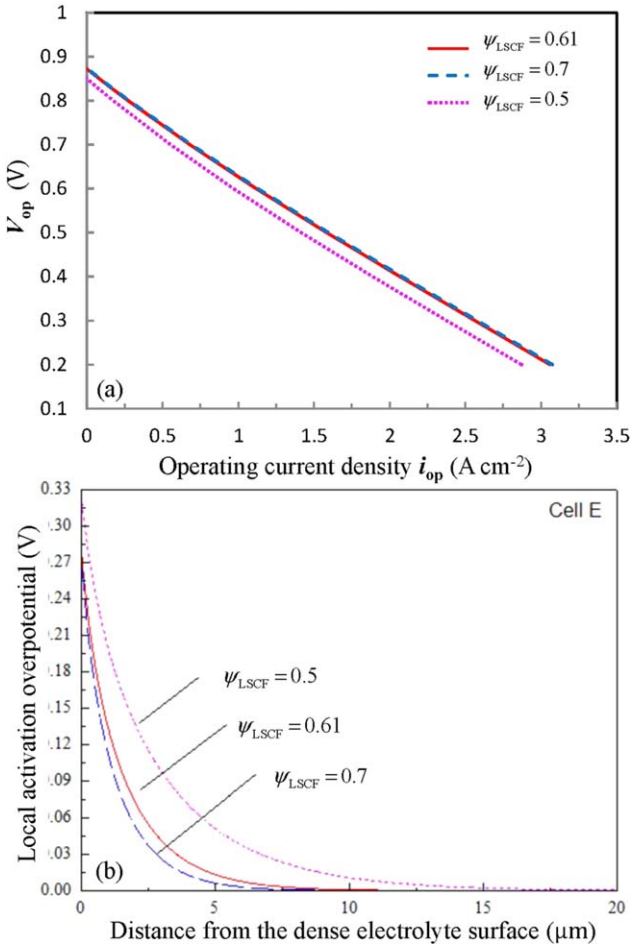


**Figure 10. The effects of three different LSCF loading on, (a) the Cell E performances, (b) local $\eta^{c}_{act}$ distribution within the cathode, at 600°C.**

**[Color figure can be viewed in the online issue, which is available at wileyonlinelibrary.com.]**

concusions were obtained from an analysis of the modeling results:

1. The distributions of PEAS and real EAS in the typical LSCF, LSCF-SDC, and LSCF-LSM IT-electrodes have been analyzed systematically to provide a way to easily understand the characteristics of the IT-SOFC electrodes containing mixed conducting materials;

2. Various appropriate constraint relationships between the activation overpotential expressions and electric boundary condition settings have been obtained by mathematically analyzing the local electrochemical equilibrium process. These are collected in Table 1 and can be used as an important reference to check the accuracy of the SOFC mathematical model parameter and boundary settings;

3. Compared with the percolated LSCF-SDC-pore TPBs, the percolated LSCF-pore DPBs in composite cathode are the dominant sites for the cathodic electrochemical reactions. The distribution of the real EAS will futher rely on the speciefic electrode characteristcs, electrode thickness, and operating conditions. For the typical IT-SOFCs using LSCF-materials, a 10-$\mu$m cathode thickness is sufficient to support most of the cathode electrochemical reactions; the remainder of the cathode zone is inactive;

4. Although the internal electronic leaking of the IT electrolyte materials (i.e., SDC) greatly reduces the OCV and

increases fuel/oxygen consumptions, its effects on the IT-SOFC performance in the typical operating region are quite small, especially for cases with the high operating current;

Generally, the developed and validated multiscale model can be applied to various SOFCs with mixed conducting materials, not only limited to LSCF-SDC/SDC/Ni-SDC SOFCs. It can also be further used to investigate the effects of various compositions, microstructure parameters, and working conditions on the electrode characteristic properties, and further on the working details within the SOFC to provide guidelines for optimizing of SOFC performance.

## Acknowledgments

The authors gratefully acknowledge the financial support of the National Natural Science Foundation of China (21106058), the Jiangsu Province Qinglan Project. The authors also acknowledge the financial support from Australia Research Council through project DP 150104365.

## Notation

$a_{k-l}$ = the contact area between $k$- and $l$-particles, $m^2$
BSCF = $Ba_{0.5}Sr_{0.5}Co_{0.8}Fe_{0.2}O_{3-\delta}$
$B_0$ = flow permeability, $m^2$
$c_\alpha^0$ = the concentration of species $\alpha$ at the channel inlet, mol $m^{-3}$
DPB = the LSCF-pore double phase boundary
$D_\alpha^{\text{eff}}$ = the effective diffusivity of species $\alpha$, $m^2$ $s^{-1}$
$D_{\alpha,\beta}^{\text{eff}}$ = the effective binary diffusivity, $m^2$ $s^{-1}$
$D_{\text{Kn},\alpha}^{\text{eff}}$ = the effective Knudsen diffusivity of species $\alpha$, $m^2$ $s^{-1}$
$E^{\text{eq}}$ = the local equilibrium electric potentials difference at working state, V
$E^{\text{st}}$ = the Nernst potential at the standard state, V
$E_0$ = the Nernst potential based on species concentrations on the inlets, V
$E_{H_2}$ = the activation energy for $H_2$ oxidation reaction, J
$E_{O_2}$ = the activation energy for $O_2$ reduction reaction, J
EAZ = the real electrochemical active sites
$F$ = Faraday constant, C $mol^{-1}$
GDC = $Gd_{0.1}Ce_{0.9}O_{1.95}$
$j_{\text{TPB}}$ = the local $e^-$-$O^{2-}$ charge transfer rate per unit TPB length, A $m^{-1}$
$j_{\text{TPB},0}$ = the local exchange transfer current per unit TPB lengths, A $m^{-1}$
$i_e$ = the local $e^-$ electric current density, A $m^{-2}$
$i_{O^{2-}}$ = the local $O^{2-}$ electric current densities, A $m^{-2}$
$i_{\text{op}}$ = the output current density, A $m^{-2}$
$i_{\text{leak}}$ = the internal leakage electronic current density, A $m^{-2}$
$i_{\text{LSCF}}$ = the $e^-$-$O^{2-}$ charge transfer rate per unit percolated DPB area, A $m^{-2}$
$i_{\text{LSCF},0}$ = the local exchange transfer current per unit percolated DPB area, A $m^{-2}$
$i_{e\text{-}O^{2-},\text{TPB}}^{\text{V}}$ = the $e^-$-$O^{2-}$ charge transfer rate per unit volume based on percolated TPBs, A $m^{-3}$
$i_{e\text{-}O^{2-},\text{LSCF}}^{\text{V}}$ = the $e^-$-$O^{2-}$ charge transfer rate per unit volume based on percolated LSCF-pore DPBs, A $m^{-3}$
$i_{e\text{-}O^{2-},\text{TPB}}^{\text{S}}$ = the $e^-$-$O^{2-}$ charge transfer rate per unit dense electrolyte surface, A $m^{-2}$
LSCF = $La_{0.6}Sr_{0.4}Co_{0.2}Fe_{0.8}O_{3-\delta}$
LSM = $La_{1-x}Sr_xMnO_3$
$M_\alpha$ = the mole mass of species $\alpha$, kg $mol^{-3}$
$N_\alpha$ = the molar flux of species $\alpha$, mol $m^{-2}$ $s^{-1}$
$n_k^{\text{V}}$ = the number of $k$-particles per unit volume
$n_k^{\text{S}}$ = the number of $k$-particles per unit dense electrolyte surface area
PEAS = the potential electrochemical active sites
$p_\alpha$ = the partial pressure of gas species $\alpha$ at the local reaction sites, atm
$p_\alpha^0$ = the partial pressure of gas species $\alpha$ in the channel inlet, atm
$P_k^{\text{i}}$ = the probabilities of $k$-particles belonging to percolated ionic conducting path
$P_k^{\text{e}}$ = the probabilities of $k$-particles belonging to percolated $e^-$ conducting path
$r_g$ = the mean hydraulic pore radius of porous electrode structure, m
$r_k$ = the radius of $k$-particle, m
$r_c$ = the neck radius between two connected particles, m
$R$ = the universal gas constant, J $mol^{-1}$ $K^{-1}$
$R_\alpha$ = the sources/leak of species $\alpha$, mol $m^{-3}$ $s^{-1}$
SDC = $Sm_{0.2}Ce_{0.8}O_{2-\delta}$
SFMO = $SrFe_{0.75}Mo_{0.25}O_{3-\delta}$
$S_{\text{es,LSCF}}$ = the percolated LSCF-pore DPBs per unit volume, $m^{-1}$
$s_{\text{es}}$ = the exposed surface area of each LSCF-particle, $m^2$
$T$ = operating temperature, K
TPB = three phase boundary sites
$V_{\text{op}}$ = the output voltage at working state, V
$v_\alpha$ = the diffusion volume for species $\alpha$, $m^3$ $mol^{-1}$
$x_\alpha$ = the molar fraction of species $\alpha$
YSZ = yttria-stabilized zirconia
$Z_{k,l}$ = the average number of contacts between $k$-particle and all of its neighboring $l$-particle
$\bar{Z}$ = the average coordination number of all particles

### *Greek letters*

$\alpha_f$, $\beta_r$ = the forward and reverse reaction symmetric factors
$\gamma_{\text{LSCF, SDC}}$ = the 1-D circular length per contact between LSCF- and SDC-particles, m
$\gamma_{\text{LSCF, ele}}$ = the 1-D circular length per contact between LSCF-particle and the dense electrolyte, m
$\delta_{k-l}$ = the thickness of the individual interface between $k$- and $l$-particles, m
$\lambda_{\text{TPB,eff}}^V$ = the percolated TPB length per unit volume, $m^{-2}$
$\lambda_{\text{TPB,eff}}^S$ = the percolated TPB length per dense electrolyte surface area, $m^{-1}$
$\phi_g$ = the porosity of porous structure
$\Phi_e$ = the local $e^-$ electric potential, V
$\Phi_{O^{2-}}$ = the local $O^{2-}$ electric potential, V
$\hat{\Phi}_e$ = the shift of $\Phi_e$ by a reference amount, V
$\hat{\Phi}_{O^{2-}}$ = the shift of $\Phi_{O^{2-}}$ by a reference amount, V
$\psi_k$ = the solid volume fraction of $k$-particles
$\eta_{\text{act}}$ = the local activation overpotential, V
$\theta$ = the smaller contact angle between two particles (Figure 1a)
$\theta_{\text{LSCF}}$ = the contact angles between $r_{\text{LSCF}}$- and $r_2$-particles (Figure 1c)
$\tau$ = the tortuosity of gas transport path within the porous electrode
$\sigma_e^{\text{eff}}$ = the effective electronic conductivity, S $m^{-1}$
$\sigma_{O^{2-}}^{\text{eff}}$ = the effective $O^{2-}$ ionic conductivity, S $m^{-1}$
$\sigma_{k-l}^{\text{i,tet,eff}}$ = the effective interparticle ionic conductivity among $k$- and $l$-particles, S $m^{-1}$
$\sigma_{mat}^{\text{tra,eff}}$ = the effective intraparticle conductivity based on geometry
$\sigma_{mat}^{\text{tra,0}}$ = the instinct electric conductivity of *mat*-material in a dense solid, S $m^{-1}$
$\mu$ = the viscosity of gas mixture, kg $m^{-1}$ $s^{-1}$
$\mu_\alpha$ = the mole chemical potential of reactant $\alpha$, J $mol^{-1}$

### *Superscripts and subscripts*

a = anode
act = activation
c = cathode
eq = equilibrium
st = standard condition (1 atm)
ref = reference value

## Literature Cited

1. Wachsman ED, Lee KT. Lowering the temperature of solid oxide fuel cells. *Science*. 2011;334(6058):935–939.
2. Suzuki T, Hasan Z, Funahashi Y, Yamaguchi T, Fujishiro Y, Awano M. Impact of anode microstructure on solid oxide fuel cells. *Science*. 2009;325(5942):852–855.
3. Shao ZP, Haile SM. A high-performance cathode for the next generation of solid-oxide fuel cells. *Nature*. 2004;431(7005):170–173.
4. Dokamaingam P, Laosiripojana N, Soottitantawat A, Assabumrungrat S. Alternative concept for SOFC with direct internal reforming operation: benefits from inserting catalyst rod. *AIChE J*. 2010;56(6):1639–1650.

5. Jayakumar A, Javadekar A, Gissinger J, Vohs JM, Huber GW, Gorte RJ. The stability of direct carbon fuel cells with molten Sb and Sb–Bi alloy anodes. *AIChE J*. 2013;59(9):3342–3348.
6. Shi H, Su C, Yang G, Ran R, Hao Y, Tade MO, Shao Z. Fabrication and operation of flow-through tubular SOFCs for electric power and synthesis gas cogeneration from methane. *AIChE J*. 2014;60(3): 1036–1044.
7. Jian L, Bin H, Wenying Z. Metallic Interconnect Materials of Solid Oxide Fuel Cells, in Materials for High-Temperature Fuel Cells In: Jiang SP and Yan Y, editors. Weinheim, Germany: Wiley-VCH Verlag GmbH & Co. KGaA, 2013. doi: 10.1002/9783527644261.ch5.
8. Wu L, Zhao L, Zhan Z, Xia C. Cathode supported tubular solid oxide fuel cells with nanostructured $La_{0.6}Sr_{0.4}Co_{0.2}Fe_{0.8}O_3$ electrocatalysts. *J Power Sources*. 2014;266:268–274.
9. Li C, Chen H, Shi H, Tade MO, Shao Z. Green fabrication of composite cathode with attractive performance for solid oxide fuel cells through facile inkjet printing. *J Power Sources*. 2015;273:465–471.
10. Wang F, Wang A, Chen J, Chi B, Pu J, Jian L. Comparative study of Pd and PdO as cathodes for oxygen reduction reaction in intermediate temperature solid oxide fuel cells. *Int J Hydrogen Energy*. 2014;39(26):14421–14427.
11. Ni M, Leung MKH, Leung DYC. Theoretical analysis of reversible solid oxide fuel cell based on proton-conducting electrolyte. *J Power Sources*. 2008;177(2):369–375.
12. Zhang C, Grass ME, McDaniel AH, DeCaluwe SC, Gabaly FE, Liu Z, McCarty KF, Farrow RL, Linne MA, Hussain Z, Jackson GS, Bluhm H, Eichhorn BW. Measuring fundamental properties in operating solid oxide electrochemical cells by using in situ X-ray photoelectron spectroscopy. *Nat Mater*. 2010;9(11):944–949.
13. Hong T, Zhang L, Chen F, Xia C. Oxygen surface exchange properties of $La_{0.6}Sr_{0.4}Co_{0.8}Fe_{0.2}O_{3-\delta}$ coated with $Sm_xCe_{1-x}O_{2-\delta}$. *J Power Sources*. 2012;218:254–260.
14. Wang S-F, Wang Y-R, Yeh C-T, Hsu Y-F, Chyou S-D, Lee W-T. Effects of bi-layer $La_{0.6}Sr_{0.4}Co_{0.2}Fe_{0.8}O_{3-\delta}$-based cathodes on characteristics of intermediate temperature solid oxide fuel cells. *J Power Sources*. 2011;196(3):977–987.
15. Bao C, Shi Y, Li C, Cai N, Su Q. Mathematical modeling of solid oxide fuel cells at high fuel utilization based on diffusion equivalent circuit model. *AIChE J*. 2010;56(5):1363–1371.
16. Gaiselmann G, Neumann M, Schmidt V, Pecho O, Hocker T, Holzer L. Quantitative relationships between microstructure and effective transport properties based on virtual materials testing. *AIChE J*. 2014;60(6):1983–1999.
17. Wiedenmann D, Keller L, Holzer L, Stojadinović J, Münch B, Suarez L, Fumey B, Hagendorfer H, Brönnimann R, Modregger P, Gorbar M, Vogt UF, Züttel A, Mantia FL, Wepf R, Grobéty B. Three-dimensional pore structure and ion conductivity of porous ceramic diaphragms. *AIChE J*. 2013;59(5):1446–1457.
18. Suwanwarangkul R, Croiset E, Entchev E, Charojrochkul S, Pritzker MD, Fowler MW, Douglas PL, Chewathanakup S, Mahaudom H. Experimental and modeling study of solid oxide fuel cell operating with syngas fuel. *J Power Sources*. 2006;161(1):308–322.
19. Zhang Y, Sun Q, Xia C, Ni M. Geometric properties of nanostructured solid oxide fuel cell electrodes. *J Electrochem Soc*. 2013; 160(3):F278–F289.
20. Leah RT, Brandon NP, Aguiar P. Modelling of cells, stacks and systems based around metal-supported planar IT-SOFC cells with CGO electrolytes operating at 500–600°C. *J Power Sources*. 2005;145(2):336–352.
21. Cui D, Liu Q, Chen F. Modeling of anode-supported SOFCs with samaria doped-ceria electrolytes operating at 500–600°C. *J Power Sources*. 2010;195(13):4160–4167.
22. Shen S, Guo L, Liu H. An analytical model for solid oxide fuel cells with bi-layer electrolyte. *Int J Hydrogen Energy*. 2013;38(4):1967–1975.
23. Shimonosono T, Hirata Y, Ehira Y, Sameshima S, Horita T, Yokokawa H. Electronic conductivity measurement of Sm-and La-doped ceria ceramics by Hebb–Wagner method. *Solid State Ionics*. 2004;174(1):27–33.
24. Ohayre RP, Cha SW, Colella W, Prinz FB. Fuel Cell Fundamentals. New York: John Wiley & Sons, 2006.
25. Chen D, Bi W, Kong W, Lin Z. Combined micro-scale and macro-scale modeling of the composite electrode of a solid oxide fuel cell. *J Power Sources*. 2010;195:6598–6610.
26. Kee RJ, Zhu H, Goodwin DG. Modeling electrochemistry and solid-oxide fuel cells: I. Basic principles. *J Combust Soc Jpn*. 2005;47: 192–204.
27. Costamagna P, Honegger K. Modeling of solid oxide heat exchanger integrated stacks and simulation at high fuel utilization. *J Electrochem Soc*. 1998;145(11):3995–4007.
28. Zhu HY, Kee RJ. Modeling distributed charge-transfer processes in SOFC membrane electrode assemblies. *J Electrochem Soc*. 2008; 155(7):B715–B729.
29. Jeon DH, Nam JH, Kim CJ. Microstructural optimization of anode-supported solid oxide fuel cells by a comprehensive microscale model. *J Electrochem Soc*. 2006;153(2):A406–A417.
30. Liu SX, Song C, Lin ZJ. The effects of the interconnect rib contact resistance on the performance of planar solid oxide fuel cell stack and the rib design optimization. *J Power Sources*. 2008;183(1):214–225.
31. Matsui T, Inaba M, Mineshige A, Ogumi Z. Electrochemical properties of ceria-based oxides for use in intermediate-temperature SOFCs. *Solid State Ionics*. 2005;176(7):647–654.
32. Zhang X, Robertson M, Deĉes-Petit C, Qu W, Kesler O, Maric R, Ghosh D. Internal shorting and fuel loss of a low temperature solid oxide fuel cell with SDC electrolyte. *J Power Sources*. 2007;164(2): 668–677.
33. Todd B, Young JB. Thermodynamic and transport properties of gases for use in solid oxide fuel cell modelling. *J Power Sources*. 2002;110(1):186–200.
34. Chen D, Lin Z, Zhu H, Kee RJ. Percolation theory to predict effective properties of solid oxide fuel-cell composite electrodes. *J Power Sources*. 2009;191:240–252.
35. Suzuki M, Oshima T. Estimation of the co-ordination number in a multi-component mixture of spheres. *Powder Technol*. 1983;35:159–166.
36. Costamagna P, Costa P, Antonucci V. Micro-modelling of solid oxide fuel cell electrodes. *Electrochim Acta*. 1998;43(3–4):375–394.
37. Chan SH, Chen XJ, Khor KA. Cathode micromodel of solid oxide fuel cell. *J Electrochem Soc*. 2004;151(1):A164–A172.
38. Bertei A, Nicolella C. Percolation theory in SOFC composite electrodes: effects of porosity and particle size distribution on effective properties. *J Power Sources*. 2011;196(22):9429–9436.
39. Farhad S, Hamdullahpur F. Optimization of the microstructure of porous composite cathodes in solid oxide fuel cells. *AIChE J*. 2012; 58(4):1248–1261.
40. Chen D, He H, Zhang D, Wang H, Ni M. Percolation theory in solid oxide fuel cell composite electrodes with a mixed electronic and ionic conductor. *Energies*. 2013;6:1632–1656.
41. Wu JJ, McLachlan DS. Percolation exponents and thresholds obtained from the nearly ideal continuum percolation system graphite-boron nitride. *Phys Rev B*. 1997;56(3):1236–1248.
42. Verkerk MJ, Middelhuis BJ, Burggraaf AJ. Effect of grain boundaries on the conductivity of high-purity $ZrO_2$-$Y_2O_3$ ceramics. *Solid State Ionics*. 1982;6(2):159–170.
43. Esquirol A, Kilner J, Brandon N. Oxygen transport in $La_{0.6}Sr_{0.4}Co_{0.2}Fe_{0.8}O_{3-\delta}$/$Ce_{0.8}Ge_{0.2}O_{2-x}$ composite cathode for IT-SOFCs. *Solid State Ionics*. 2004;175(1–4):63–67.
44. Yu JH, Park GW, Lee S, Woo SK. Microstructural effects on the electrical and mechanical properties of Ni-YSZ cermet for SOFC anode. *J Power Sources*. 2007;163(2):926–932.

*Manuscript received Dec. 19, 2014, and revision received Apr. 17, 2015.*